Applied Catalysis B: Environment and Energy 361 (2025) 124666

Contents lists available at ScienceDirect

Applied Catalysis B: Environment and Energy

journal homepage: www.elsevier.com/locate/apcatb

Higher-valent nickel oxides with enhanced two-electron oxygen reduction in advanced electro-Fenton system for organic pollutants degradation

Wenjun Zhang [a,b,1], Thao Thi Le [c,1], Dongyup Shin [d,1], Subhajit Nandy [e], Jae Won Choi [a], Sae Yane Paek [a,f], Chang-Kyu Hwang [a,g], Jin Hyueng Kim [a,h], Hoyoung Suh [e], Keun Hwa Chae [e], Seung Yong Lee [a], Sang Soo Han [d,*], Sang Hoon Kim [b,c,i,**], Jong Min Kim [a,b,i,***]

[a] Materials Architecturing Research Center, Korea Institute of Science and Technology (KIST), Seoul 02792, Republic of Korea
[b] Division of Nanoscience and Technology, KIST School, University of Science and Technology (UST), Seoul 02792, Republic of Korea
[c] Extreme Materials Research Center, Korea Institute of Science and Technology (KIST), Seoul 02792, Republic of Korea
[d] Computational Science Research Center, Korea Institute of Science and Technology (KIST), Seoul 02792, Republic of Korea
[e] Advanced Analysis Data Center, Korea Institute of Science and Technology (KIST), Seoul 02792, Republic of Korea
[f] Department of Energy Engineering, Hanyang University, Seoul 04763, Republic of Korea
[g] Department of Micro/Nano System, Korea University, 145 Anam-ro, Seongbuk-gu, Seoul 02841, Republic of Korea
[h] Department of Materials Science and Engineering, Korea University, 145 Anam-ro, Seongbuk-gu, Seoul 02841, Republic of Korea
[i] KHU-KIST Department of Converging Science and Technology, Kyung Hee University, Seoul 02447, Republic of Korea

ARTICLE INFO

Keywords:
Higher-valent nickel oxide
Hydrogen peroxide production
Oxygen reduction reaction
Flow cell electro-Fenton
Wastewater treatment

ABSTRACT

A higher-valent NiO catalyst, enriched with trivalent Ni (Ni^{3+}) and exposed {111} crystal facets, was developed to enhance selective two-electron oxygen reduction ($2e^-$ ORR) for electrochemical hydrogen peroxide (H_2O_2) production, leading to highly efficient organic pollutant removal. The catalyst was synthesized via a precipitation method, incorporating crystal facet and cation vacancy engineering to expose active sites. It demonstrated 96 % selectivity and 59 A g^{-1} mass activity, attributed to weakened *OOH binding, as shown by density functional theory. Integrated into an advanced electro-Fenton (EF) flow cell, the system achieved 100 % removal of 200 mL of 50 ppm bisphenol A (BPA) in 4 minutes, with 93 % total organic carbon removal within 2 hours. This study provides a scalable and efficient solution for decentralized environmental remediation and wastewater treatment.

1. Introduction

In recent years, the escalating global scarcity of clean water, exacerbated by numerous persistent and toxic contaminants, poses a significant threat to all creatures, increasing the risk of infections and facilitating the spread of diseases. This underscores the urgent need for access to safe water in modern society [1]. Non-biodegradable and long-lasting estrogen-like compounds, phenolic endocrine disruption chemicals (EDCs), can rapidly decrease human reproductive capacity by influencing multiple endocrine-related pathways. They may also increase cancer risks and interact with other substances in aquatic environments to produce harmful compounds, causing severe health issues even at low concentrations [2,3]. One of the notable representatives among various EDCs, bisphenol A (BPA) is highly accessible in aquatic systems due to its ubiquity in multiple products such as medical equipment, electronic manufacturing, building coatings, and product packaging. It is thus necessary to develop effective wastewater treatment techniques for such recalcitrant pollutants [4,5].

BPA can, in principle, be eliminated by advanced oxidation processes such as conventional Fenton and Fenton-like reactions [6–9]. However, degradation processes up to complete mineralization are reported to be slow and ineffective. Considerable research efforts have been invested to improve the performance. Among these efforts, on the basis of *in situ* hydrogen peroxide (H_2O_2) production and energy utilization,

* Corresponding author.
** Corresponding author at: Division of Nanoscience and Technology, KIST School, University of Science and Technology (UST), Seoul 02792, Republic of Korea.
*** Corresponding author at: Materials Architecturing Research Center, Korea Institute of Science and Technology (KIST), Seoul 02792, Republic of Korea.
E-mail addresses: sangsoo@kist.re.kr (S.S. Han), kim_sh@kist.re.kr (S.H. Kim), jongminkim@kist.re.kr (J.M. Kim).
[1] These authors contributed equally to this work.

https://doi.org/10.1016/j.apcatb.2024.124666
Received 4 June 2024; Received in revised form 19 September 2024; Accepted 30 September 2024
Available online 1 October 2024

electro-Fenton (EF) processes have been actively studied recently [10–12]. EF is an oxidation reaction between added ionic Fe and in-situ obtained H_2O_2 to generate hydroxyl radicals (•OH) ($Fe^{2+} + H_2O_2 + H^+ \rightarrow Fe^{3+} + H_2O + \cdot OH$) during the electrocatalytic process of the two-electron oxygen reduction reaction ($2e^-$ ORR, $O_2 + H^+ + e^- \rightarrow {}^*OOH$, ${}^*OOH + H^+ + e^- \rightarrow H_2O_2$) [13,14]. By utilizing the catalytic reaction for H_2O_2 production in the cathodic part, the EF system can decompose durable toxicants into smaller molecules with activated •OH radicals from the produced H_2O_2 and regenerated ferrous ions. Despite the effectiveness of the EF process, challenges arise in achieving fast and complete removal of concentrated pollutants in large quantities [15,16]. This is because, EF kinetics are heavily controlled by the H_2O_2 production rate catalyzed at the cathode, while in non-flowing degradation devices such as a batch reaction or an H-type cell, the produced H_2O_2 would undergo self-decomposition over extended cell operation, thereby decreasing •OH generation and hindering mineralization [17]. To address these challenges, developing highly efficient and robust $2e^-$ ORR electrocatalysts is essential while designing more advanced electrochemical cell assemblies that allow for the mass production of H_2O_2 and simultaneous Fenton reactions.

The $2e^-$ ORR catalysts have predominantly relied on carbon materials. However, considering the acidic Fenton environment, carbon-based materials exhibit inadequate catalytic activity at low pH values [18–21]. This would lead to carbon degradation and demetallation, which has been identified as the main contributor to significant active site depletion [22–24]. To address these limitations, abundant and cost-effective earth resources, particularly non-noble transition metal oxides, are considered promising candidates for $2e^-$ ORR catalysts. The electric field effect on the surface of transition metal oxides makes breaking O–O bonds challenging, which favors the "end-on" adsorption mode of O_2 over the "side-on" mode. This hinders the cleavage of O–O bonds, thereby enhancing the selectivity for the $2e^-$ ORR pathway [25,26]. Moreover, as inorganic materials, they are relatively resistant to •OH attack [27,28]. In recent years, extensive research has optimized the intrinsic properties of metal oxides by altering their composition, crystallinity, and introducing defects to enhance their catalytic activity and selectivity for the $2e^-$ ORR. However, achieving satisfactory levels of both activity and selectivity remains a formidable task [29–32]. Among various transition metal oxides, NiO has recently emerged as a $2e^-$ ORR catalyst through amorphous structure to induce end-on O_2 adsorption, enhancing $2e^-$ ORR properties compared to crystalline forms [33,34]. However, the amorphous nature limits active cation density, creating a trade-off between crystallinity and H_2O_2 performance. Increasing crystallinity boosts O_2 adsorption sites but conflicts with $2e^-$ ORR selectivity. Decreasing crystallinity, on the other hand, enhances $2e^-$ ORR selectivity but reduces active sites [35,36]. In other words, this trade-off in NiO is seen as a hurdle to overcome for its utilization as a $2e^-$ ORR catalyst material, and it clearly shows that this trade-off cannot be resolved by crystallinity control alone. To overcome the aforementioned limitations and achieve balanced selectivity and activity for the $2e^-$ ORR in NiO, defect engineering can be explored as an alternative strategy. In this regard, there are diverse examples demonstrating the potential of high-valence state cation defects on NiO surfaces to improve catalytic properties in various catalytic reactions[37–41]. However, to the best of our knowledge, the simultaneous control of the crystal facet and surface defects in NiO catalysts for highly active and selective $2e^-$ ORR has not been reported to date.

In addition, from a system perspective, since the O_2 supplied in the conventional EF reaction system relies mostly on low concentrations of dissolved O_2 in an electrolyte, the level of produced H_2O_2 is very low [42]. Furthermore, as the reaction typically occurs in a batch system, the generated H_2O_2 is not effectively utilized for pollutant removal due to its self-decomposition. In this regard, to maximize the water treatment efficiency of the EF process, there is a critical need to develop both outstanding transition metal catalysts for the $2e^-$ ORR and advanced electrochemical cell designs capable of maximizing H_2O_2 production.

In this study, we developed a high-performance NiO catalyst with nickel vacancies (NivO) by carefully controlling the facets and vacancies. And utilized this catalyst in an advanced EF system, demonstrating its effectiveness in degrading high concentrations of persistent pollutants. Here, the synthesized {111}-NivO, a trivalent nickel (Ni^{3+})-rich NiO with surface exposure of the (111) facet, was synthesized by a precipitation method involving crystal facet and cation vacancy engineering. The catalyst exhibits an ultra-high selectivity of up to 96 % and an impressive mass activity of 59 A g^{-1}, which far exceeds all other Ni-based catalysts reported in the literature. Density functional theory (DFT) computational studies indicate that for the (111) surface of NiO, which tends to form Ni vacancies, an increase in the concentration of these vacancies leads to weaker binding of the *OOH intermediate species. In addition, excellent $2e^-$ ORR performance is confirmed through a flow cell device with Faradaic efficiencies (FE) of >85 % in various pH conditions under a long-term stability test. Moreover, an advanced EF system when combined with a flow cell for electrochemical H_2O_2 mass production enables 100 % removal of large amounts of highly concentrated BPA pollutants (200 mL at 50 ppm) with high efficiency. Specifically, the process demonstrates an exceptionally rapid 100 % degradation of BPA within 4 min with a remarkably high kinetics value in pseudo-first-order reaction (k = 1.125 min^{-1}), marking approximately 102 times greater efficiency than that of the batch-type EF system. Additionally, the system shows competitive total organic carbon removal (TOC), reaching 93 % within 2 h.

2. Materials and methods

2.1. Chemicals

Nickel (II) sulfate hexahydrate ($NiSO_4 \cdot 6\ H_2O$, ≥99 %), oxalic acid dihydrate ($C_2H_2O_4 \cdot 2\ H_2O$, ≥99 %), sodium hydroxide (NaOH, ≥98 %), and commercial nickel (II) oxide (NiO, 99.99 % trace metals basis) were purchased from Sigma Aldrich. Potassium hydroxide (KOH, 93 %), sodium sulfate anhydrous (Na_2SO_4, 99 %), methyl alcohol (CH_3OH, 99.5 %), and phenol (>99 %) were purchased from Daejung Chemical. Sodium carbonate (Na_2CO_3, 99~100.5 %) was obtained from Samchun Chemical Co., Ltd. Sulfuric acid (H_2SO_4, 98 %) was purchased from Baker Analyzed™ A.C.S. Reagent. Carbon black KetjenBlack DJ-600 was purchased from the fuel cell store. Bisphenol A (BPA, 97 %) was purchased from Alfa Aesar.

2.2. Synthesis of {100}-NivO

In a typical synthesis[9], 0.02 mol acid precipitation agent of $C_2H_2O_4 \cdot 2\ H_2O$ was dissolved in 50 mL of deionized water under magnetic stirring, gradually reaching a solution temperature of 50°C in an oil bath. Simultaneously, under ambient conditions, 0.02 mol of $NiSO_4 \cdot 6\ H_2O$ was dissolved in 50 mL of deionized water. The resulting nickel sulfate solution was then added dropwise to the oxalate solution under vigorous stirring without pH correction. After 30 min, a turquoise precipitate formed, and the solution was transferred to an ice bath to reduce underwent calcination in an air environment at 1000°C for 1 h with a heating rate of 10°C min^{-1}, labeled as {100}-NivO or referred to as NiO-1000–10-a, denoting the synthesis conditions. The same experimental procedures were replicated by varying the pyrolysis temperature from 500 to 1000°C, resulting in NiO-500–10-a, NiO-800–10-a, NiO-900–10-a, NiO-1000–2-a, and NiO-1000–15-a, each named-based on the product, heat treatment temperature, heating rate, and the species of precipitation agent. For example, "NiO-500–10-a" denotes the sample treated at 500°C with a heating rate of 10°C min^{-1} using acid as the precipitate agent.

2.3. Synthesis of {111}-NivO

By a precipitation method for NiO synthesis, a pH of 13.4 base solution was created by a 25 mL mixture of Na_2CO_3 (0.34 mol L^{-1}) and NaOH (1.2 mol L^{-1}) aqueous solution, using magnetic stirring at room temperature. Simultaneously, a 0.51 mol L^{-1} of $NiSO_4$ solution was formed by dissolving $NiSO_4{\cdot}6\ H_2O$ in 25 mL deionized water. Gradually, this precursor solution was added incrementally to the above-mentioned base solution. The resulting mixture was stirred at room temperature for 30 minutes. The precipitated nickel hydroxide ($Ni(OH)_2$) suspension underwent heating at 50°C with continuous stirring for 2.5 days in an oil bath. Subsequently, a light-green powder was obtained through centrifuge separation and removal of the aqueous supernatant. The powder was multiple-rinsed with distilled water, followed by additional centrifugation. The final product was dried at 70°C under vacuum conditions. It was then heated in an air-filled box furnace at a rate of 10°C min^{-1} until reaching 1000°C, maintained for 1 hour, resulting in the NiO-1000–10-b sample, also designated as {111}-NivO. For a comparative analysis, Ni precipitates made by base precipitation were also subjected to altered heating temperatures (500–1000°C) and ramping speeds (2 and 15°C min^{-1}), producing NiO-500–10-b, NiO-800–10-b, NiO-900–10-b, NiO-1000–2-b and NiO-1000–15-b, respectively.

2.4. Materials characterization

Scanning electron microscopy (SEM) was conducted with a FEI Inspect F50 microscope at 10 kV to characterize the materials. Transmission electron microscopy (TEM) techniques including selected area electron diffraction (SAED), high-resolution TEM (HRTEM), and energy dispersive X-ray spectroscopy (EDS) mapping were used on a Tecnai G2 operated at 200 kV to further analyze the structure and composition. X-ray absorption fine structure (EXAFS) data were measured at 1D XRS KIST-PAL beamline in Pohang Accelerator Laboratory and processed with IFEFFIT software to obtain Fourier-transformed Ni K-edge spectra. X-ray diffraction (XRD) patterns were collected using a Rigaku Smartlab diffractometer with a Cu Kα source at 40 kV to determine the crystalline phases present. A 532 nm Renishaw Raman spectrometer was employed to analyze vibrational modes. X-ray photoelectron spectroscopy (XPS) on a ThermoFisher Nexsa system was carried out to examine surface chemical states. Electron paramagnetic resonance (EPR) spectra acquired with a 77 K Bruker-A300 spectrometer at 9.45 GHz band gave information on unpaired electrons. Optical absorption was measured by UV–vis spectroscopy on a Varian Cary 300 spectrophotometer at 319 nm.

2.5. Electrochemical measurements

A standard three-electrode cell consisting of a rotating ring disk electrode (RRDE) setup and an Autolab potentiostat (PGSTAT302N, Metrohm Autolab USA) was used for electrochemical testing. The working electrode was an RRDE with a 0.196 cm^2 glassy carbon disk and a 0.072 cm^2 platinum ring, having a determined collection efficiency of 0.250 based on a potassium ferricyanide redox system [43,44]. The counter and reference electrodes were platinum wire and Ag/AgCl in 0.1 M KOH electrolyte), while in 0.1 M Na_2SO_4 electrolyte and 0.1 M H_2SO_4 acidified Na_2SO_4 (pH 3), a saturated calomel electrode (SCE) was used as the reference electrode. Potentials were converted to the reversible hydrogen electrode (RHE) scale ($E_{RHE} = E_{Ag/AgCl} + 0.197 + 0.059 \times pH$, and $E_{RHE} = E_{SCE} + 0.241 + 0.059 \times pH$). Catalyst ink was prepared by dispersing 3 mg of a NiO/KB mixture of the synthesized NiO commercial Ketjenblack EC-600JD (KB, Fuel Cell Store) in a mass ratio of 1:1 into a solution of 1.8 mL ethanol and 50 μL of 5 wt% Nafion. The ink was then drop-cast onto the RRDE disk as the working electrode. The loading amount was varied from 10, 20, and 50 μg cm^{-2} for performance optimization. Electrochemical ORR measurements were conducted at room temperature in an O_2 pre-saturated electrolyte. Prior to the oxygen reduction reaction (ORR) measurements, the disk electrode was conditioned with cyclic voltammetry (CV) in the Ar-purged electrolyte. Ten cycles were run from 0.05 to 1.0 V at a 100-mV s^{-1} scan rate. Additional CV cycles (20 cycles, 0.1–1 V vs. RHE, 50 mV s^{-1}) were then conducted on the ring electrode to stabilize the CV response. After this initial conditioning, ORR polarization curves were obtained using linear sweep voltammetry (LSV). The measurements were conducted at 1600 rpm rotation speed without *iR* compensation. The disk potential was swept at 10 mV s^{-1} scan rate while holding the ring at a fixed 1.20 V vs. RHE over a 0.05 V range. Testing was performed in oxygen-saturated electrolytes. Here, current density (J, mA cm^{-2}) was determined from LSV polarization curves of corrected disk current (I_d, mA) and ring current (I_r, mA) in Ar-saturated and O_2-saturated electrolytes using Eqs. (1) and (2) :

$$J_d = I_d / A_d \tag{1}$$

$$J_r = I_r / (A_d \times N) \tag{2}$$

H_2O_2 selectivity (%), electron transfer number (n), and mass activity (A g^{-1}) were calculated sequentially with Eq. (3–5) below:

$$Selectivity(100\%) = 200 \times (I_r/N)/(I_d + I_r/N) \tag{3}$$

$$Electron\ transfer\ number(n) = 4 \times I_d/(I_d + I_r/N) \tag{4}$$

Here, the collection efficiency (N) of the RRDE electrode was determined to be 0.25 by measuring the redox of hexacyanoferrate ($[Fe(CN)_6]^{3-}$/$[Fe(CN)_6]^{4-}$) [43].

Kinetic current density (J_k, mA cm^{-2}) was then corrected for mass transport losses:

$$I/J_m = 1/J_l + 1/J_k \tag{5}$$

Here, J_m (mA cm^{-2}) denotes the measured total current density (which can be substituted with J_d, the disk current density). J_l (mA cm^{-2}) is the diffusion-limited current density. Obtaining the limiting current is often difficult because it requires measurement across the whole potential range, which can be addressed by combining the Levich Eq. with the total number of electrons transferred (n), determined from the rotating ring-disk electrode (RRDE) system. The Levich Eq. is as follows (Eq. (6)):

$$J_l = 0.62nFD_0^{2/3}\omega^{1/2}\upsilon^{-1/6}C_0 \tag{6}$$

Here, F is the Faraday constant with a value of 96,485 C mol^{-1}. D_0 represents the diffusion coefficient of oxygen in the electrolyte at 298 K, which is 1.85×10^{-5} cm^2 s^{-1} in 0.1 M KOH. ω is the electrode rotation speed of the electrode (rad s^{-1}). υ is the kinematic viscosity of the electrolyte, measured 0.89×10^{-2} cm^2 s^{-1} here. C_0 stands for the bulk concentration of O_2 in the electrolyte, given as 1.21×10^{-6} mol cm^{-3}.

The Tafel slopes b (mV dec^{-1}) were also acquired from the value of J_k as the Eq. (7):

$$E = C + b\log(J_k) \tag{7}$$

where E and C represent the applied potential (V vs. RHE), constant related to exchange current density (mA cm^{-2}).

To assess intrinsic electrochemical activity, the electrochemical surface area (ECSA) was determined from the active catalytic site density, computed using double-layer capacitance and C_{dl} values (Eq. (8)):

$$ECSA = C_{dl}/C_s \tag{8}$$

where C_s is the specific capacitance with a value of 40 μF cm^{-2} in 0.1 M KOH electrolyte. Here, C_{dl} (mF cm^{-2}) can be generated by Eq. (9):

$$j = C_{dl} \times \nu \tag{9}$$

where j (mA cm^{-2}) is the current density and ν is the scan rate (mV s^{-1}), making ECSA proportional to C_{dl}, derived from the predicted slope of the $j-\nu$ curve. Resistance assessment via electrochemical impedance

spectroscopy (EIS) involved Nyquist plots at 0.75 V vs. RHE with an RRDE electrode rotation of 1600 rpm in O_2-saturated electrolyte after pre-cleaning the disk of part by CV scanning in Ar gas for 20 cycles from 0.05 to 1.0 V at a scan rate of 100 mV s^{-1}, which provides the information of the initial resistance from the electrolyte (R_s, Ω), the resistance of the passive film or corrosion products on the catalyst layer surface (R_c, Ω), charge transfer resistance (R_{ct}, Ω), constant phase element with the capacitance (Q_c, μF cm^{-2}), and electric double-layer capacitor (Q_{ct}, μF cm^{-2}).

2.6. DFT computational details

Spin-polarized density functional theory (DFT) calculations were performed using the Vienna Ab initio Simulation Package (VASP) with the Perdew-Burke-Ernzerhoff (PBE) exchange-correlation functional [43]. To describe the interaction between ions and electrons, the projector-augmented-wave pseudopotentials were used [43]. Hubbard U correction was considered to minimize the self-interaction error of 3*d* transition metal oxides, and the *U* value for the Ni 3*d* orbital was set to 6.4 eV. The energy cutoff was set to 650 eV for bulk and 400 eV for slab models, respectively. In particular, an energy cutoff of 500 eV was chosen for single-point calculations to perform the partial density of state (PDOS) and partial Hessian calculations. For the NiO bulk structure, the rock-salt crystal structure was optimized with a Monkhorst–Pack k-point mesh of 15×15×15. Two different slab models, {100}-NiO and {111}-NiO, were then optimized using the Monkhorst–Pack scheme and Γ-centered k-point mesh of 5×5×1, respectively. The {100}-NiO slab models were constructed with four layers of 2×2-unit cells, where the bottom two layers were frozen during the structure optimization. The {111}-NiO slab models were designed with six layers of 3×3-unit cells, where only the top three layers were allowed to relax during the structure optimization. In the case of Ni_2O_3 models, a monoclinic Ni_2O_3 crystal structure was chosen for a bulk structure, where the bulk structure was optimized with a Γ-centered k-point mesh of 7 × 11 × 11. A {100}-Ni_2O_3 slab model with three layers was then constructed from the optimized bulk structure. For all slab models, an additional vacuum layer of 20 Å was considered and a dipole correction was employed along the normal direction.

The vacancy formation energies per atom of Ni (ΔE_{vac} (Ni), eV) and (ΔE_{vac} (O), eV) were defined as given in Eq. (10):

$$\Delta E_{vac}(Ni/O) = \frac{E_{SCF}(N*vac) - E_{SCF}(pris) + N \times \mu(\mathrm{Ni/O})}{N} \quad (10)$$

Here, N is the number of vacancies, and E_{SCF} *(vac)* (eV) and E_{SCF} *(pris)* (eV) are the electronic self-consistent field energy of the surface slabs with/without vacancy, respectively. μ (Ni/O) represents the chemical potential of Ni or O. For μ (O), the entropy term ($T\Delta S$) of the gaseous O_2 molecule was corrected to account for the synthesis temperature (1273.15 K). Similarly, the O passivation energy (ΔE_{pas} (O), eV) was obtained from Eq. (11) below:

$$\Delta E_{pas}(\mathrm{O}) = \frac{E_{SCF}(N*O) - E_{SCF}(pris) + N \times \mu(\mathrm{O})}{N} \quad (11)$$

where N is the number of absorbed oxygen atoms and E_{SCF} (O) (eV) is the electronic self-consistent field energy of the oxygen-absorbed surface slab.

To obtain the reaction-free energy under the aqueous environment, an implicit solvation model was introduced. The Poisson-Boltzmann implicit solvation model, which was implemented in the VASPsol package, was used to describe the implicit water solvent of which the corresponding dielectric constant was 78.4. The solvation effect coupled Gibbs free energies (G_{sol}, eV) were calculated according to Eq. (12):

$$G_{sol} = E_{SCF} + ZPE - T\Delta S_i + \Delta E_{sol} \quad (12)$$

where ΔE_{sol} (eV) is the solvation energy of the system, *ZPE* is the zero-point energy, and $T\Delta S_i$ is the entropic correction of vibration, rotation, and translation at 298.15 K. For the gas-phase species, the solvation effect was not considered. Furthermore, only the vibrational entropy was considered for the OOH intermediate (*OOH).

2.7. Flow cell test

To evaluate the H_2O_2 production rate, faradaic efficiency, and stability, we utilized a 6.5 × 6.5 cm^2 three-electrode flow cell system connected to a potentiostat (SP-150, Biologic). The cell consists of two compartments: an anode compartment, where the oxygen evolution reaction (OER) occurs, and a cathode compartment for ORR. These compartments are separated by a membrane. For the ORR, the working electrode was prepared by sonicating a catalyst ink containing 3 mg of catalyst, 50 μL of 5 % Nafion solution, and 2.25 mL of ethanol for 30 minutes. This ink was then spray-coated onto a 2.3 × 2.3 cm^2 piece of commercial carbon paper gas diffusion media (Sigracet 39 BB, Fuel Cell Store) at a loading of 0.3 mg cm^{-2}, followed by drying at 80°C. The actual working area of the electrode that contacts the electrolyte was 2 cm^2. In a 1 M alkaline solution made by KOH pellets with a pH of 14, a Hg/HgO electrode was used as the reference electrode, and a NiFeMo foil served as the counter electrode. The proton exchange membrane employed was the Nafion® N-117, produced by Fuel Cell Store. O_2 was continuously supplied to the cathode compartment at a rate of 20 mL min^{-1}, and the electrolyte flow rate was maintained at 40 mL min^{-1} in both the cathode and anode compartments.

Applying constant current densities ranging from 10 to 300 mA cm^{-2} induced H_2O_2 generation, catholyte samples were collected, neutralized, and titrated against a Ce^{4+} solution to quantify the H_2O_2 produced (e.g. $2Ce^{4+} + H_2O_2 \rightarrow 2Ce^{3+} + 2\,H^+ + O_2$).[45] In the previously reported procedure, a Ce^{4+} titrant was prepared by dissolving $Ce(SO_4)_2$ in 0.5 M H_2SO_4 to form a 0.6 mM standard solution and calibrated against UV–vis absorption spectra from 800 to 300 nm to generate a standard curve at 319 nm based on the Eq. (13):

$$Abs = \varepsilon \times l \times [Ce^{4+}] \quad (13)$$

where *Abs* is the absorbance at 319 nm, $[Ce^{4+}]$ is the Ce^{4+} concentration (mM), ε is the molar absorptivity of Ce^{4+} (mM^{-1} cm^{-1}), and l is the path length (cm).

After 1 hour of electrolysis in the flow cell device, a quantitative aliquot of the working electrode compartment electrolyte at a certain applied current (5 μl for 20–400 mA, 1 μl for 600 mA) was sampled and injected into 4.5 mL of standard Ce^{4+} stock solution in 0.5 M H_2SO_4.

The H_2O_2 concentration (mol L^{-1}) in the electrolyte after the ORR electrolysis was calculated using the Eq. (14):

$$H_2O_2\ concentration = \frac{[Ce^{4+}]_{Before} - [Ce^{4+}]_{after}}{2 \times V_{titration}} \times 4.5 \quad (14)$$

Here, $V_{titration}$ (mL) denotes the volume of the electrolyte taken from 40 mL KOH electrolyte for titration, where the $[Ce^{4+}]_{Before}$ and $[Ce^{4+}]_{after}$ absorbances of the Ce^{4+} stock solution at 319 nm before and after injecting the H_2O_2-containing aliquot, respectively. Since the total working electrolyte is 40 mL, the H_2O_2 yield (mol) is calculated as Eq. 15

$$H_2O_2\ yield = H_2O_2\ concentration \times 40 \quad (15)$$

Faradaic efficiency (*FE*, %) was described by Eq. (16):

$$FE = \frac{100 \times 2 \times 96485 \times H_2O_2\ yield}{\int_0^t I dt} \quad (16)$$

where $\int_0^t I dt$ stands for the cumulative charge (C) passed during electrolysis.

The H_2O_2 production rate (mol g^{-1} h^{-1}) can be calculated by Eq. (17)

$$H_2O_2 \text{ production rate} = \frac{H_2O_2 \text{ yield}}{\text{catalyst loading}} \quad (17)$$

To assess the stability, a 500 mL electrolyte solution containing 1 M KOH was continuously circulated through the electrochemical cell. This was achieved with a consistent flow rate of 40 mL min^{-1} and a constant O_2 flow rate of 20 mL min^{-1}. Constant current testing at 200 mA over 36 h was conducted with 100 % IR compensation every 1 h. Similarly, the H_2O_2 performance test and stability measurement in neutral solution (1 M Na_2SO_4, pH=7) and acid electrolyte (0.5 M H_2SO_4 adjusted 1 M Na_2SO_4, pH=3) were carried out following the same procedure in the alkaline electrolyte by only changing the counter electrode in the OER electrocatalyst with Ir foil and the reference electrode with an Ag/AgCl electrode.

2.8. Flow cell type EF degradation of pollutants

Electron-Fenton degradation experiments were conducted using a flow cell setup. The setup consisted of an Ir foil as the counter electrode, a {111}-NivO/KB ink mixture (with a 1:1 mass ratio of {111}-NivO to KB) spray-coated on a GDL as the working cathode, and an Ag/AgCl electrode as the reference. The ink preparation conditions were consistent with those used in the flow cell test, with catalyst loading varied at 0.2, 0.6, and 0.9 mg cm^{-2}. 50 ppm Bisphenol A (BPA) in the electrolyte of O_2-saturated acidified 1 M Na_2SO_4 (pH 3) was circulated only in the cathode part during H_2O_2 production for degradation, and was vigorously stirred at 400 rpm, operating under different current densities of 100, 200, and 400 mA. Notably, to mitigate Fe^{2+} precipitation caused by pH changes during in-situ H_2O_2 production, the electrolyte pH was continuously adjusted by adding acid to maintain it at approximately pH 3 throughout the 2-hour reaction. Fenton catalyst Fe^{2+} was introduced at concentrations of 0.3, 1.3, and 1.5 mM, respectively. Purged O_2 flow rates were varied at 10-, 20-, and 40-mL min^{-1}. To determine BPA concentration, small aliquots (0.6 mL) were taken at specific intervals and promptly measured using a high-performance liquid chromatography (HPLC) machine equipped with a Shim-pack GIS C18 column (4.6 × 150 mm, Agilent) at 40°C and a UV/Vis detector. The mobile phase, a 40:60 (v/v) mixture of methanol and water, flowed at 1.0 mL min^{-1}, with an injection volume of 50 μL at $\lambda = 270$ nm. The mineralization assessment was quantified on a TOC analyzer (multi N/C, 3100) from 10 mL aliquots at intervals using a standard non-permeable organic carbon method (NPOC). The BPA degradation efficiency (BPA_{de}, %) was calculated using the provided Eq. (18), and the corresponding first-order rate constant (k) of BPA degradation was derived from the linear fitting of time-dependent BPA concentration alternation for the quantitative comparison the pseudo-first-order kinetic of the reaction from Eq. (19), and TOC removal (%) was calculated according to Eq. (20):

$$BPA_{de} = \frac{[BPA]_0 - [BPA]_t}{[BPA]_0} \times 100 \quad (18)$$

$$\ln\left(\frac{[BPA]_t}{[BPA]_0}\right) = -kt \times 100 \quad (19)$$

$$TOC\ removal = \frac{[TOC]_0 - [TOC]_t}{[TOC]_0} \times 100 \quad (20)$$

where $[BPA]_0$ (mg L^{-1}) and $[TOC]_0$ (ppm) is the initial concentration of the BPA solution, $[BPA]_t$ (mg L^{-1}) and $[TOC]_t$ (ppm) is the concentration of the BPA solution during the reaction at time t (min), and k (min^{-1}) is the first-order rate constant.

3. Results and discussion

3.1. Synthesis and characterizations of materials

Using a precipitation method, NiO with controlled exposed crystal facets and maximized trivalent nickel (Ni^{3+}) content arising from Niv was successfully synthesized. As illustrated in Fig. 1a, various NiO structures are produced by gradually forming green precipitates upon adding precipitation agents to a nickel (II) sulfate hexahydrate ($NiSO_4{\cdot}6\ H_2O$) solution, followed by air calcination at different temperatures (see more details in the Experimental Section). NiO morphologies annealed from 500°C to 1000°C at 10°C min^{-1} heating rate, were studied using scanning electron microscopy (SEM), high-resolution transmission electron microscopy (HRTEM), selected area electron diffraction (SAED) patterns, and energy-dispersive X-ray spectroscopy (EDS) mapping. Specifically, taking NiO produced by acid precipitation under different heating conditions as an example (Figs. S1-S7 and Table S1), a noticeable morphological evolution is observed. Irregular polycrystalline particles with an average crystal size of 23.94 nm are formed at 500°C. While cubic-like particle aggregates appear at 800°C, single crystal cuboid NiO with high density (100) facet exposure gradually forms from 900 to 1000°C, showing an increased crystal size of 64.10 nm. Simultaneously, the Ni^{3+} cation content increases progressively, induced by Ni^{2+} vacancies maintaining charge neutrality across samples ($1/2\ O_2^{(g)} \leftrightarrow O_O^x + V''_{Ni} + 2\ h^+$, $Ni^{2+} + h^+ \rightarrow Ni^{3+}$, where O_O^x is an oxygen atom on the NiO lattice site and V''_{Ni} is a Ni^{2+} vacancy) [38]. This was confirmed by X-ray photoelectron spectroscopy (XPS) spectra (Fig. S8 and Table S2). Particularly in the {100}-NivO sample treated at 1000°C with a ramping speed of 10 °C min^{-1}, the abundance of higher-valent Ni reaches its maximum. In contrast, when maintaining a high pyrolysis temperature of 1000°C, using a slower heating rate of 2 °C min^{-1} allows for a more prolonged interaction with O_2 in the air. This extended exposure provides sufficient time for structural reformation and atomic rearrangement, resulting in a more uniform and stable oxidation process. Consequently, the (100) crystal facet dominated NiO with fewer cation vacancies is formed (as indicated by a decrease in the relative atomic ratio of Ni^{3+} to Ni^{2+} from 3.16 to 2.25, based on deconvoluted Ni2p XPS spectra; see Figs. S8-S10).

This suggests that the precipitation method for NiO synthesis, conducted at high temperatures with rapid heating, can facilitate fast crystallization and surface diffusion, promoting the formation of vacancies. However, when a faster heating rate of 15°C min^{-1} is applied, the resulting NiO retains the same exposed {100} crystal facet but shows a slightly reduced Ni^{3+}/Ni^{2+} atomic ratio of 2.8 (Fig. S11 and S12). This slight reversal may be attributed to the accelerated temperature increase, which could induce internal stress, leading to structural reformation and rearrangement of surface atoms during calcination. These adjustments may result in a more stable surface structure by reducing the number of coordinatively unsaturated Ni atoms, particularly those at edges and corners [46].

Pyrolysis of an alkaline precipitate solution containing aqueous nickel sulfate was also conducted in the air under the same pyrolysis condition for validation (Fig. S13-S19 and Tables S3-S4). Similarly, only polycrystalline NiO aggregates with 44.5 nm average size formed at 500°C. From 800°C, polyhedron growth gradually occurred, with some evident hexagonal-like octahedrons. At 1000°C, a complete transformation into highly dense irregular octahedrons was observed (Figs. 1b-1g). The SAED pattern and the HRTEM images depicted in Fig. 1h and Fig. 1i suggest a single-crystalline cubic structure, with heptagonal-like surfaces having four long sides parallel to {111} NiO planes along the [110] zone axis, indicating dominant exposed {111} facets in the synthesized {111}-NivO. The {111}-NivO exhibited a similar abundance of Ni^{2+} vacancies as {100}-NivO, with a maximized Ni^{3+} content (relative Ni^{3+}/Ni^{2+} ratio reaches to 3.25). However, when the heating rate was reduced to 2°C min^{-1}, the Ni^{3+}/Ni^{2+} ratio decreased to 2.48 (Fig. S20-S21 and Table S4). Conversely, increasing the heating rate to 15°C min^{-1} led to a decrease in the relative amount of defects in the resulting {100}-NivO sample, with the Ni^{3+}/Ni^{2+} ratio at 3.05, showing a trend similar to that of {100}-NivO produced under the same conditions (Fig. S22-S23).Thus, it can be concluded that a heating rate of 10°C min^{-1} is optimal for forming a highly cation-defective structure,

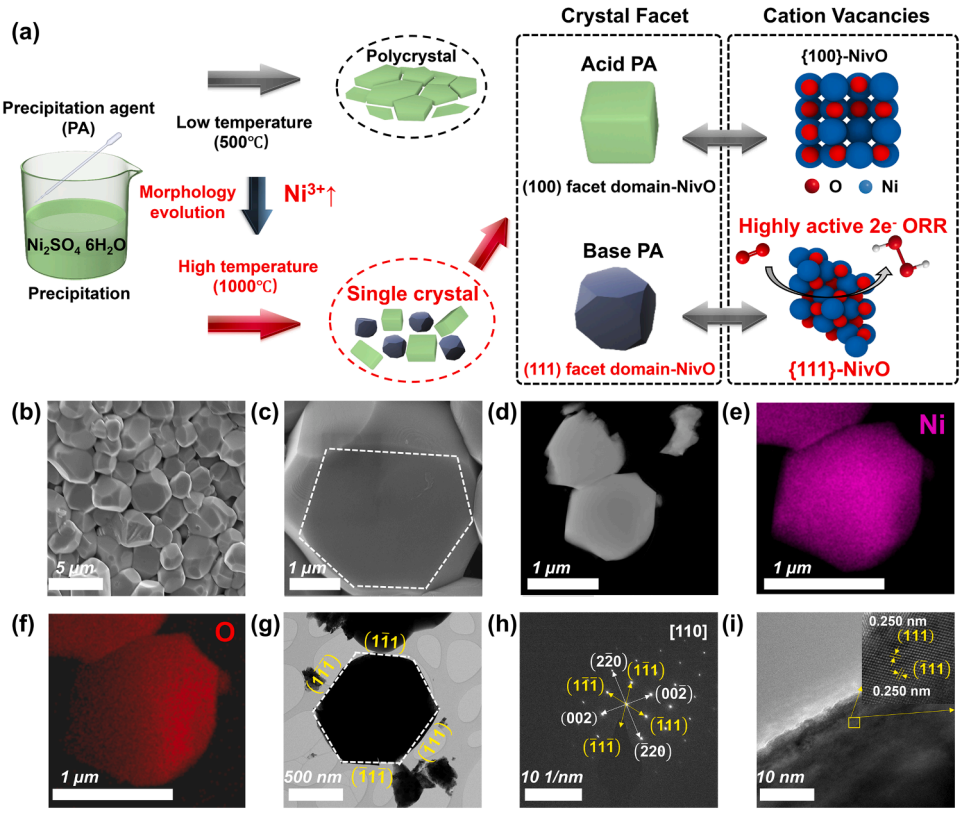

Fig. 1. Strategy for crystal facet and defect engineering of NiO based on control of precipitation agent and synthesis temperature. (a) Schematic illustration of the synthesis process for NivO. (b, c) SEM images, (d-f) EDS element mapping images, (g) TEM image, (h) SAED pattern, and (i) HRTEM image of {111}-NivO.

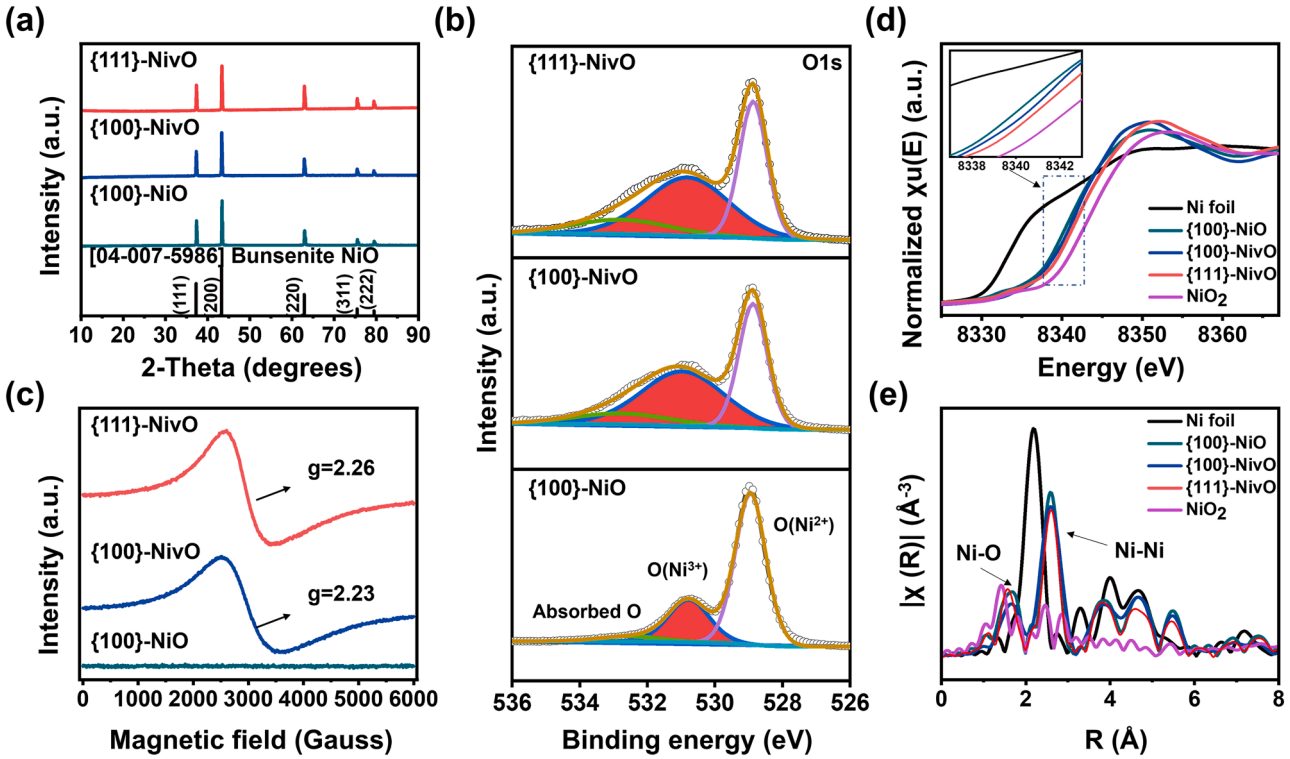

Fig. 2. Material characterization of the obtained NiO samples and their references. (a) XRD pattern. (b) Deconvoluted XPS O 1 s spectra. (c) EPR spectra and their calculated g factor of {100}-NiO, {100}-NivO, and {111}-NivO. (d) The normalized XANES spectra at Ni K-edge. (e) Fourier-transform EXAFS spectra in R space of {100}-NiO, {100}-NivO, and {111}-NivO and their references.

promoting the creation of single crystals and maximizing the introduction of Ni vacancies (Niv).

It is known that under oxygen-rich conditions, the predominant defect in NiO is the nickel vacancy [47]. In the case of rapid crystallization at high temperatures, the observed effect can be elucidated by rearrangements within the surface layer, wherein the nickel ions migrate into the bulk of the crystal, thereby creating cationic vacancies. The charge associated with these vacancies is compensated by an elevated concentration of Ni^{3+} species [48]. This underscores the influence of high temperature and a rapid pyrolysis rate on the optimal inclusion of Ni cation defects in NiO. For comparison, a commercially available stoichiometric (100) facet-exposed NiO cuboid, {100}-NiO, was also employed (Fig. S24 and S25). Despite sharing the same cubic structure as the bunsenite NiO reference and exhibiting nearly identical crystal sizes (~64.7 nm for {100}-NiO, ~64.1 nm for {100}-NivO, ~67.1 nm for {111}-NivO), as determined by an XRD analysis (Fig. 2a and Table S5). The precise compositions of different Ni species were further quantitatively examined to identify the presence of Niv in various NiO samples using XPS. Although the distinction between samples is noticeable in both Ni2p and O1s spectra, directly illustrating the Ni^{3+}/Ni^{2+} ratio is complicated and obscured in the Ni 2p spectrum due to the presence of multiple overlapped Ni^{2+}, Ni^{3+} peaks, and satellite Ni signals. However, clearer differences indicative of Ni^{2+} and Ni^{3+} chemical bonds are evident in the O1s spectra at approximately 529 and 531 eV, corresponding to O binding with nearby Ni^{2+} and Ni^{3+}, respectively [49]. As illustrated in Fig. 2b and Table S5, except physisorbed H_2O on the NiO surface (~533 eV), visible differences exist in the peak area of O(Ni^{3+}) and the relative atomic ratio of O(Ni^{3+}) and O (Ni^{2+}) species (O(Ni^{3+})/O(Ni^{2+})). The O(Ni^{3+})/O(Ni^{2+}) ratios are similar for {100}-NivO and {111}-NivO (1.27 and 1.3), but approximately 3.3 times higher than that in {100}-NiO (0.38), indicating more defects in the produced catalysts versus commercial compounds. Additionally, different fitting ratios of Ni^{3+} and Ni^{2+} species (Ni^{3+}/Ni^{2+}) in the deconvoluted peaks of Ni2p spectra between the Ni^{2+} state (binding energies: ~853 eV and 871 eV) and Ni^{3+} state (binding energies: ~855 eV and 874 eV) shows the real Niv diversities in the NiO samples (3.25 for {111}-NivO, 3.16 for {100}-NivO, and 2.31 for {100}-NiO), implying the higher possibility of Niv in {111}-NivO and {100}-NivO rather than commercial {100} NiO-reference (Fig. S26) [40].

To further characterize the defects in NiO, we used electron paramagnetic resonance (EPR) spectroscopy. This technique measures the g factor, determined by the resonance frequency of a paramagnetic substance, to identify and quantify the unpaired electrons in different forms of NiO [50]. As expected, {111}-NivO and {100}-NivO exhibit much stronger EPR signals, arising from unpaired localized Ni electrons compared to {100} NiO, with prominent signals of g values at 2.26 and 2.23, respectively. This verifies that Niv is dominantly present in these two samples. At the same time, pristine NiO shows a lack of Ni defects, as no signal was observed in EPR (Fig. 2c and Fig. S27) [51]. Furthermore, Ni K-edge X-ray absorption near edge spectroscopy (XANES) and extended X-ray absorption fine structure (EXAFS) spectra were also measured to disclose the real coordination environment for various forms of NiO and other Ni-based references. As depicted in Fig. 2d, the near-edge absorption energy of all the samples is located within the range of those of Ni and

NiO_2 references, indicating that their positive valence state is between +0 and +4. However, in contrast to the {100} facet domain of NiO, both {100}-NivO and {111}-NivO exhibit comparably higher Ni binding energy shifts in the absorption edge (blue dashed box), and stronger peak intensity (red dashed box), suggesting higher average oxidation states of Ni due to the existence of larger contents of high-valent Ni^{3+}. This is consistent with the higher Ni^{3+}/Ni^{2+} ratios observed in the XPS analysis. Furthermore, the distinctly lower peak intensity at the higher coordinated 2nd Ni-Ni shell in the R-space for {111}-NivO and {100}-NivO, compared to {100}-NiO, strongly implies the formation of nickel vacancies (Fig. 2e and Fig. S28). Additionally, the simulated structural parameters from quantitatively fitted EXAFS spectra in the nickel K-edge (Table S6) reveal that the mean coordination numbers of Ni-Ni in {111}-NivO and {100}-NivO are around 11 and 11.4, respectively, which are lower than that of commercial NiO bulk (11.8 in stoichiometric {100}-NiO). This is direct evidence of the existence of Niv. Moreover, the decreased distances in the 1st shell of Ni-O and the 2nd shell of Ni-Ni in {111}-NivO, and a decrease in the Ni-O bond distance and an increase in the Ni-Ni distance for {100}-NivO, all confirm the presence of nickel defects derived from high-temperature crystallization on different exposed crystal planes on the surface of NiO [52–54].

As reported, Niv are well recognized as primary point defects in synthesized NiO, while oxygen vacancies (Ov) also emerge from air environment calcination conditions [49,55]. Despite the absence of obvious peak splits in the EPR spectra for Ni and O defects, the potential presence of dual vacancies in varying amounts is feasible due to the close signal positions (the g factor is approximately 2 for Ov and 2.1–2.3 for Niv) [31,49,51,56]. Notably, the absorption edge of the {111}-NivO is slightly positively shifted (blue dashed box). This indicates a higher amount of hypervalent-state Ni^{3+} existed in {111}-NivO than in {100}-NivO, which is consistent with the absolute content of Ni^{3+} observed in XPS analyses (Fig. 2b and Table S5). The EXAFS fitting results in Fig. S29 and Table S6 also reveal a slightly lower coordination number between Ni and O in the case of {100}-NivO compared to {111}-NivO and commercial {100}-NiO samples (5.7 for {100}-NivO, 5.9 for {111}-NivO and 6 for {100}-NiO). This lower value indicates the possibility that Ov are created and accumulate around Ni in {100}-NivO. In addition, further support can be obtained from EXAFS spectra with a lower intensity for the 1st shell Ni-O in {100}-NivO, indirectly indicating a minor amount of Ov (Figs. 2b, 2e, Fig. S28 and Table S6). It is known that under O-rich conditions for NiO crystallization, the formation of Ni-defective crystals is energetically preferred over those with O defects (~38 eV for Niv and ~9 eV for Ov) [31,57]. However, considering the different exposed surfaces for {100}-NivO and {111}-NivO, the formation energy of Niv and Ov can be regulated. For NiO exposed to a large amount of (100) planes, introducing a small amount of Ov together with predominated Niv simultaneously allows more stable lattice configurations, while the formation of Ov on the (111) facet is challenging, whether in isolation or within a Niv-rich environmentas confirmed by the subsequent DFT simulations.

3.2. Electrocatalytic ORR performance evaluation

The excellent H_2O_2 production performance of {111}-NivO was confirmed by a three-electrode system utilizing a RRDE. The tests were conducted at a rotational speed of 1600 rpm in an O_2-saturated electrolyte. Here, to compensate for low conductivity and to eliminate the effects of differing electrical conductivities among the various NiO samples, all samples were initially physically mixed with carbon black (Ketjenblack EC 600JD (KB)) in a 1:1 ratio to achieve uniform charge transfer resistance (Fig. S30 and Table S7). The catalyst loading was optimized at 20 μg cm^{-2}, striking a balance between high selectivity and large current densities (Fig. S31). In the ORR polarization curves measured in a 0.1 M KOH electrolyte with a pH of 13 (Fig. 3a), {111}-NivO/KB exhibits the earliest onset potential (0.75 V vs. RHE) among various NiO- based catalysts, indicating rapid kinetics of the surface O_2/HO_2^- process. This heightened ORR activity was further evidenced by the Tafel slopes, where {111}-NivO/KB boasts the lowest slope of 50 mV dec^{-1} among various NiO-based catalysts for superior ORR kinetics (Fig. S32a). In addition, the mass-transport corrected kinetic current density for H_2O_2 production (jk, H_2O_2) on {111}-NivO/KB, estimated using the Koutecky–Levich Eq., achieves a positive current density of 2.24 mA cm^{-2} at 0.65 V vs. RHE, comparable to or even better than state-of-the-art noble-based nanoclusters (Fig. S32b). The distinct highest current densities are also observed in the ring part. This confirms the superior activity of {111}-NivO/KB, especially in the mixed-

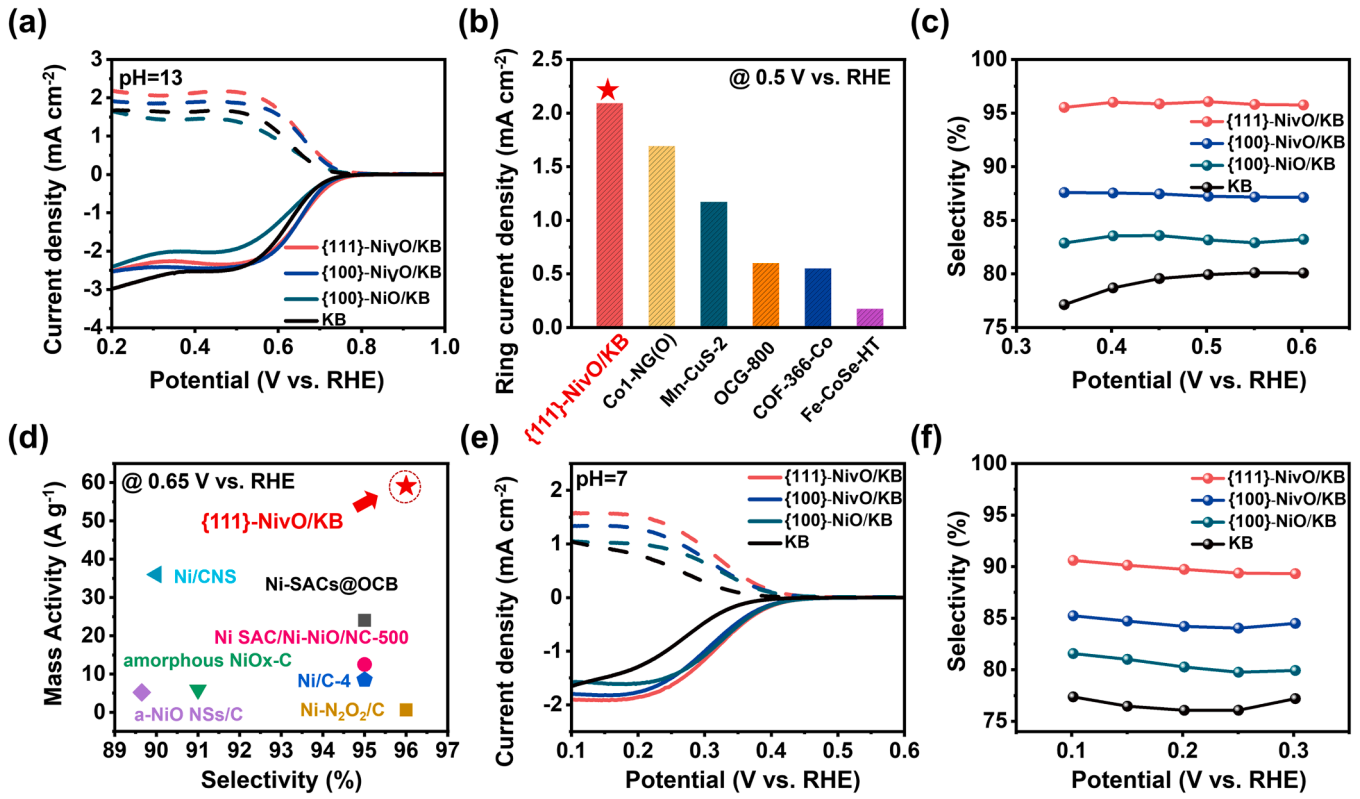

Fig. 3. The H_2O_2 performance of the catalysts by RRDE. (a) ORR polarization curves of {111}-NivO/KB, {100}-NivO/KB, {100}-NiO/KB, and KB in 0.1 M KOH. (b) Comparison of ring current density between {111}-NivO/KB obtained from the ORR curve and a reported catalyst at 0.5 V vs. RHE. (c) Calculated H_2O_2 selectivity from their ORR curves in alkaline electrolyte. (d) Comparison of the calculated mass activity of {111}-NivO /KB from the ORR curve and that of the reported Ni-based catalysts at 0.65 V vs. RHE. (e) $2e^-$ ORR polarization curves of {111}-NivO/KB, {100}-NivO/KB, {100}-NiO/KB and KB in 0.1 M Na_2SO_4. (f) Calculated H_2O_2 selectivity from their ORR curves in neutral electrolytes.

controlled area (0.4–0.6 V vs. RHE), where it displays a competitive ring current density of 2.09 mA cm^{-2} compared to well-reported non-noble-based materials at 0.5 V vs. RHE (Fig. 3b and Table S8). With up to 23 % enhanced selectivity compared to the (100)-facet exposed {100}-NiO sample, {111}-NivO/KB exhibits excellent catalytic performance, boasting 96 % ultrahigh selectivity and high mass activity of 59 A g^{-1} at 0.65 V vs. RHE in 0.1 M KOH (Fig. 3c). This performance is achieved with an approximately $2e^-$ transfer process (Fig. S33). More importantly, the outstanding balance between high selectivity and mass activity substantially surpasses all other reported Ni-based catalysts (Fig. 3d and Table S9). In contrast, pure KB exhibits 26 % lower selectivity, reduced current densities, and a significantly lower mass activity of 28 A g^{-1} compared to the {111}-NivO/KB composite. This indirectly demonstrates the positive influence of {111}-NivO on selective H_2O_2 production.

Furthermore, the {111}-NvO plays a significant role in stabilizing reaction intermediates. To confirm this, a Peroxide Reduction Reaction (PRR, $H_2O_2 + 2H^+ + 2e^- \rightarrow H_2O$) test was performed for both the KB and {111}-NivO/KB catalysts, using the same method as in the ORR test. This experiment was conducted in an Ar-saturated 0.1 M KOH electrolyte containing 10 mM H_2O_2. As shown in Fig. S34, the {111}-NivO/KB catalyst exhibits the lowest PRR current compared to other samples, indicating that the active sites of the {111}-NivO based catalyst effectively prevent the further reduction of H_2O_2. Notably, the significantly lower PRR activity of {111}-NivO/KB compared to pure KB underscores the role of {111}-NivO in the selective synthesis of H_2O_2, highlighting its superiority over KB as an electrocatalyst.

When changing the electrolyte from alkaline to neutral and acidic conditions, a similar catalytic trend is observed, with the formed {111}-NivO/KB catalyst consistently surpassing the electrocatalytic performance of other comparison catalysts. In 0.1 M Na_2SO_4 as the electrolyte, the {111}-NivO/KB composite exhibits the highest current density and approximately 90 % selectivity, which is 13 %, 8 %, and 5 % higher than that of KB, {100}-NiO/KB, and {100}-NivO/KB, respectively (Figs. 3e and 3f). In acidic conditions (Fig. S35), the {111}-NivO/KB composite similarly demonstrates the highest ring current densities and an average competitive selectivity of 93 % for H_2O_2 production compared to the other reference samples. The electrochemical transfer number in both neutral and acidic electrolyte conditions also confirms the $2e^-$ catalytic process for the optimized {111}-NivO/KB sample, with an average electron transfer number of 2.20 and 2.14 in these two electrolytes, respectively (Fig. S35 and S36). This enhanced performance underscores the beneficial influence of the {111}-NivO component for selective H_2O_2 generation across varying electrolyte pH environments.

To verify the superior performance of {111}-NivO, electrochemical surface areas (ECSA) were examined. As illustrated in Fig. S37, {111}-NivO exhibits a reduced ECSA compared to {100}-NiO and {100}-NivO, suggesting that its heightened activity and selectivity for the $2e^-$ ORR stem from the tailored crystal facet and vacancies rather than ECSA prominence. To be specific, introducing a sufficient amount of vacancy on the (100) surface in the backbone of {100}-NiO to form {100}-NivO can help enhance both disk and ring current density as well as the selectivity across the entire potential range. While further adjusting the crystal plane from (100) to (111) with high density and maximum exposure of Ni^{3+} active sites, the positive effect on ring current and selectivity can be amplified, disclosing the crucial role of crystal facet and cation vacancy engineering.

Additionally, {111}-NivO samples with the same (111) crystal facets but varying Niv content were prepared by pyrolyzing NiO at 1000°C with different ramping speeds, ranging from 2 to 15°C min^{-1}. Based on their identical exposed (111) facets and only varying ramping speeds

during synthesis, the samples were designated as {111}-NivO (2°C min^{-1}), {111}-NivO (10°C min^{-1}), and {111}-NivO (15°C min^{-1}). As shown in Fig. S38, the catalytic performance of the KB mixture with these {111}-NivO samples was evaluated, revealing a trend in enhanced current density, selectivity, and mass activity: {111}-NivO (10°C min^{-1}) > {111}-NivO (15°C min^{-1}) > {111}-NivO (2°C min^{-1}). This trend corresponds to the relative Ni^{3+}/Ni^{2+} ratios observed in the XPS analysis (Fig. S23). Similarly, samples with exposed (100) facets, prepared under the same conditions ({100}-NivO (10°C min^{-1}), {100}-NivO (15°C min^{-1}), and {100}-NivO (2°C min^{-1})), showed a consistent trend in H_2O_2 production electrocatalytic activity, underscoring the positive role of Niv as active sites for the $2e^-$ ORR (Fig. S39).

3.3. Theoretical calculations

To investigate the effect of surface vacancies and high-valent Ni active centers for the $2e^-$ ORR in NiO catalysts, density functional theory (DFT) calculations were performed. Based on the electron paramagnetic resonance (EPR) data (Fig. 2c), a NiO catalyst model with Niv was formulated, and an additional Ni_2O_3 catalyst model was considered in order to disentangle the effects of high-valent centers and vacancies (Fig. 4a). Various surface configurations, including the Ni-terminated NiO with exposed (111) surface and Niv (Ni-rich {111}-NivO), the NiO (100) surface with Ni vacancy ({100}-NivO), and the NiO (100) surface with Ni and O vacancies ({100}-NivOv), were examined to elucidate surface vacancy configurations (Fig. S40 and S41). As shown in Fig. 4b, the Ni-rich {111}-NivO exhibited a preference for a Ni vacancy-rich environment, in contrast to the {100}-NivO surface. These DFT results align with the differences in the quantity of EPR signals observed in the experiments (Fig. 2c). Additionally, the successful synthesis of Ni-terminated {111}-NivO provides further evidence of the exposed Ni surface. Moreover, DFT calculations reveal that the alterations in the NiO surface environment influence the oxidation state of Ni active centers. XPS simulation results confirm that an increase in the number of Niv leads to further oxidation of the Ni active center on both facets (Fig. 4c).

The two facets not only differ in their preference for Niv but also exhibit variations in the impact of Niv on catalytic activity. In Figs. 4d and 4e, for {111}-NivO, which favors vacancies, an increase in the number of vacancies leads to weak binding of *OOH (* denotes a surface site). Conversely, on {100}-NivO, the energetic advantage resulting from changes in vacancy number is negligible. Even on Ni vacancy-rich {100}-NivO with high oxidation states (the number of vacancies > 5) and Ni_2O_3 surface, low $2e^-$ ORR activity is predicted. This suggests that

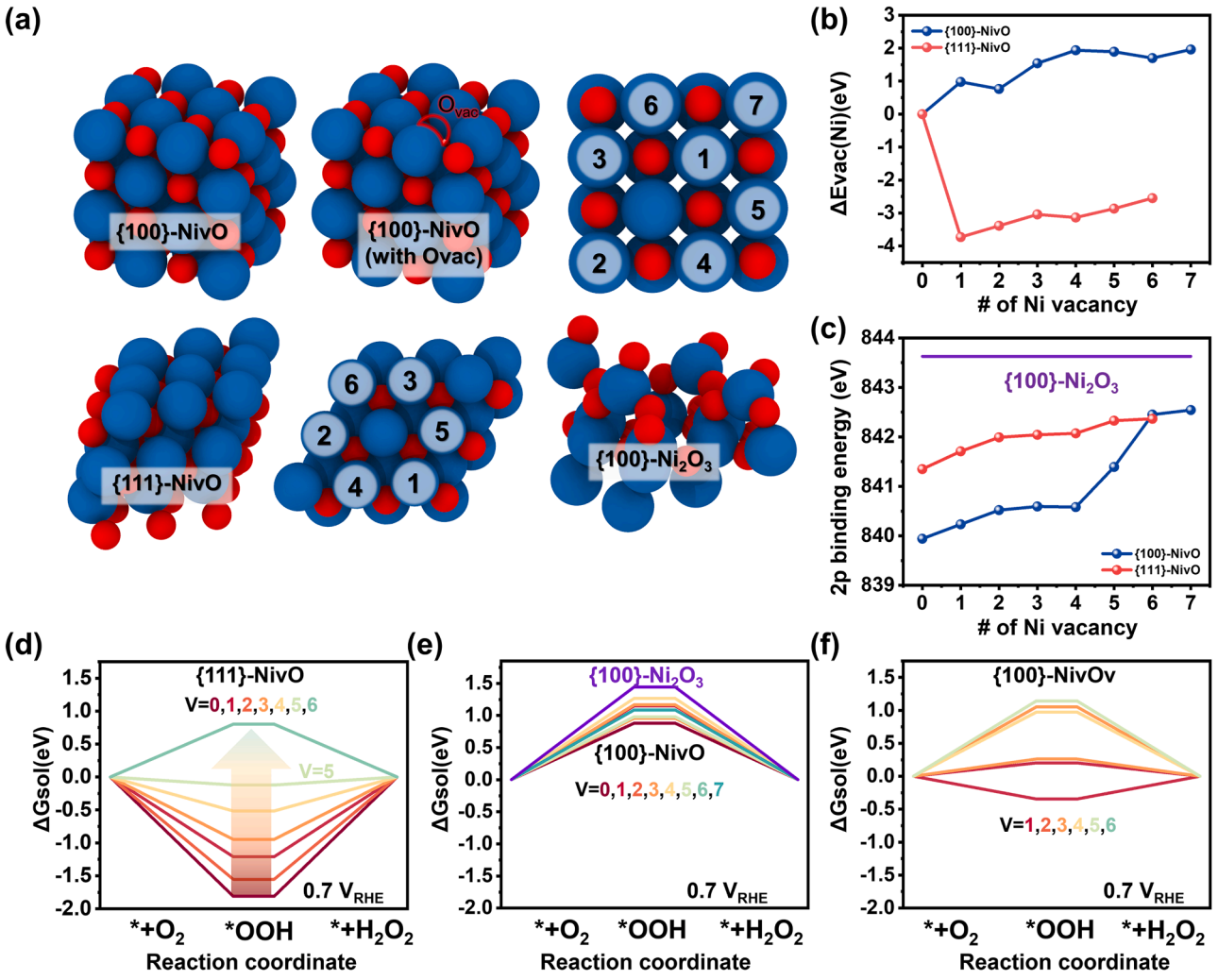

Fig. 4. DFT results of the electrochemical $2e^-$ ORR performance of the catalysts. (a) Atomic structures of various nickel oxide catalysts. The pristine structures of the NiO (100) facet (top) and NiO (111) facet and Ni_2O_3 (100) (bottom) are presented. The sequence of Niv formation, as determined through DFT calculations, is indicated by the number on the top view of (100) and (111) facets. The color code for an atom is blue = Ni and red = O. (b) The vacancy formation energy of Ni. (c) The XPS simulation data of Ni as a function of the number of Niv. (d-f) The reaction energy diagrams for Ni-rich {111}-NivO (d), {100}-NivO and {100}-Ni_2O_3 (e), and {100}-NivOv. (f) The reaction energy diagrams were plotted at 0.7 V_{RHE} (# means number of elements).

the increase in Ni oxidation states induced by defects is not a major contributing factor to the enhancement of catalytic activity. In particular, on the (111) facet, increasing the oxidation state of Ni in the absence of Ni vacancies (surface oxidation) is predicted to lead to excessively weak binding, resulting in reduced catalytic performance (Fig. S42). To explore the origin of the observed improved catalytic activity of the {100}-NivO sample in our experiments (Fig. 2a), we considered a Ni_vO_v catalyst model, where Ni and O vacancies coexist. For the clean {100}-NivO surface, the formation energy of O vacancy, ΔE_{vac} (O), was calculated to be as high as 4.41 eV, indicating that O vacancy formation is not favorable. However, as the number of Niv on {100}-NivO increases, O vacancy formation becomes readily favored (Fig. S41h). In contrast, O vacancy formation on the Ni-rich {111}-NivO surface is unlikely to be favorable, even with a high number of Niv. According to Fig. 4b, it would be difficult to find high concentrations of Niv on {100}-NivO. The cumulative ΔE_{vac} (Ni) for {100}-NivO with three Niv is 4.62 eV (3×1.54 eV), resembling the ΔE_{vac} (O) of pristine {100}-NiO. Consequently, the energetic benefit for oxygen vacancy formation diminishes beyond the presence of four Niv. Considering the energy trade-off balance, the structure of the {100}-NivO sample is speculated to involve a moderate Ni vacancy environment (i.e., the number of vacancies = 2–3) coexisting with one oxygen vacancy ({100}-NivOv). Indeed, for this case, the Ni active center exhibited a reduced overpotential on the {100}-NivOv (Fig. 4f).

To gain a comprehensive understanding of the effects of vacancies, we conducted partial density of states (PDOS) calculations for the 3*d* orbital of the Ni active center in NiO catalyst models. As depicted in Fig. S43a, the most significant difference between the two Ni PDOSs on {100}-NivO and {111}-NivO lies in the position of the d_{z2} state. On the pristine {100}-NivO, the d_{z2} state is partially occupied, with the unoccupied state contributing to bonding with the OOH intermediate (*OOH). However, the unoccupied d_{z2} is relatively far from the Fermi level, enhancing its antibonding properties and leading to the formation of energetically unstable bonds. In Fig. S44, it is confirmed that the energy level of the unoccupied d_{z2} on {100}-NivO does not significantly change with an increasing number of Niv, supporting the negligible effect of Niv on the catalytic activity for the $2e^-$ ORR on {100}-NivO shown in Fig. 4d. On the other hand, on the (111) facet, the d_{z2} state is fully occupied below the Fermi level on both pristine {111}-NivO and all Ni vacancy configurations (Fig. S45). Unlike the (100) facet, the (111) facet necessitates charge transfer from the d_{z2} state to another unoccupied state to form *OOH binding. Consequently, the charge transfer cost influences the bond strength of *OOH. Fig. S44b illustrates a scheme for the orbital interaction between *OOH and the (100) or (111) facet. As shown in Fig. S45a-d, when the vacancy density is low (the number of vacancies < 4), the empty states are near the Fermi level. However, as the vacancy density increases, the energy of the lowest unoccupied state gradually rises (1.03 eV, 1.47 eV, and 2.17 eV for 4, 5, and 6 Niv, respectively). This is consistent with the trend of the *OOH binding strength to decrease with the number of vacancies in the $2e^-$ ORR energy profile of Ni-rich {111}-NivO (Fig. 4c). The difference in the *d* orbital splitting of the Ni center due to the Ni vacancy effect on the (100) and (111) facets of NiO can be attributed to the distinction in their coordination environments. The surface Ni atoms on the (100) facet form octahedral coordination with oxygen, whereas Ni atoms on the (111) facet are situated in tetrahedral coordination. As a result, d_{z2} states contributing to binding are grouped into different orbital sets, an octahedral field of e_g and a tetrahedral field of *e*. The removal of surface Ni atoms on the (111) facet strengthens the in-plane effect of oxygen, influencing the orbital splitting excluding d_{z2}. This clarifies why Niv can enhance the ORR performance specifically on the (111) facet. The distinct differences in the positions of interaction states between Ni and *OOH, as shown in the PDOS diagrams of *OOH adsorption states on the (100) and (111) surfaces, further support this observation (Fig. S43c-f).

On the other hand, {100}-NivOv also exhibits enhanced ORR catalytic performance, although it has a Ni PDOS similar to that of {100}-NivO (Fig. S46). The improved performance is attributed to a synergistic effect. Leveraging this synergistic effect, typically arising from the spatial proximity of more than two active sites, is considered a promising strategy to reduce overpotentials by enabling more stable absorption states. This phenomenon occurs through the creation of a 'dual-single atom catalyst'-like structure, where two initially isolated Ni active sites on the (100) surface can share one intermediate due to the presence of an O vacancy. Consequently, this leads to the stabilization of the intermediate (Fig. S47). However, as discussed in Fig. S48, in the case of {100}-NivO, the *OOH binding structure remains largely unchanged even at high concentrations of Niv. The synergistic effect is also evident in the (111) facet. On pristine {111}-NivO, surface Ni atoms are not isolated, allowing for bridge or three-fold binding. Fortunately, with an increase in the number of Niv, the remaining surface Ni atoms become isolated (Fig. S49). This suggests that steric effects, influenced by changes in vacancy configuration, also play a role in affecting the binding strength of *OOH.

3.4. Practical scale H_2O_2 electrosynthesis

Based on the excellent activity of the {111}-NivO/KB catalyst confirmed by RRDE tests and DFT calculations, it is possible to mass-produce H_2O_2 when applied in a high current density-based electrochemical flow cell setup [43]. In the cell device, the working electrode in the cathode comprises three layers: a catalyst layer, a microporous layer (MPL), and a gas diffusion layer (GDL). The MPL, typically composed of carbon black and PTFE, aids in the uniform distribution of gases and prevents flooding within the gas diffusion layer. The GDL, made of carbon fiber paper, facilitates the rapid mass transfer of generated H_2O_2 while continuously supplying a large amount of O_2 gas [58]. In this setup, the {111}-NivO/KB catalyst served as the optimal cathode catalyst in a custom-made flow cell device. The production rate and faradaic efficiency (FE) of H_2O_2 were recorded under various current densities (10–300 mA cm^{-2}) with iR compensation across different pH conditions to evaluate the catalytic properties and stability of this high-valence NiO sample (The detailed cell schematic and the morphology of the working electrode are shown in Fig. S50 and S51, respectively). In both alkaline and neutral electrolytes, {111}-NivO/KB exhibits a lower overpotential across the overall potential range compared to pristine KB, attributed to excellent ORR kinetics from the RRDE analysis (Figs. 3a, 3e, and Fig. S52). In the case of the electrocatalytic performance of H_2O_2 production demonstrated in Fig. 5a-c, it is revealed that (111)-faceted NiO with rich Niv supported on KB, {111}-NivO/KB, has far superior performance as an electrocatalyst for H_2O_2 production compared to both pure KB and{100}-NiO/KB (Fig. S53). This significant enhancement is observed across tests at different pH levels. In particular, in alkaline electrolytes, our {111}-NivO/KB electrocatalyst exhibits outstanding cell-operating performance, achieving 14.8 mol g^{-1} h^{-1} of H_2O_2 with a 93 % Faradaic efficiency (FE) at a high current density of 300 mA cm^{-2} (Fig. 5a). This performance surpasses the production rates of previously reported Ni-based catalysts (Fig. S54 and Table S10) and significantly outperforms the pure GDL, which has an average selectivity of less than 60 % for H_2O_2 production due to the intrinsic properties of the carbon material used in its fabrication (Fig. S55). Over 36 h of stability testing, {111}-NivO/KB maintains ~85 % FE (Fig. S56a), showcasing promising durability. Likewise, under neutral pH conditions, {111}-NivO/KB shows a significant overpotential advantage, yielding 9.4 mol g^{-1} h^{-1} H_2O_2 at 90 % FE with 36 h stability (Fig. 5c and Fig. S56b). Even under an acidic environment, it maintains 90 % FE for at least 12 h (Fig. 5d). The enhanced performance and stability across varying pH environments suggests {111}-NivO is a promising stable electrocatalyst for unprecedented mass yield and energy-efficient H_2O_2 production among various Ni-based electrocatalysts [59–62].

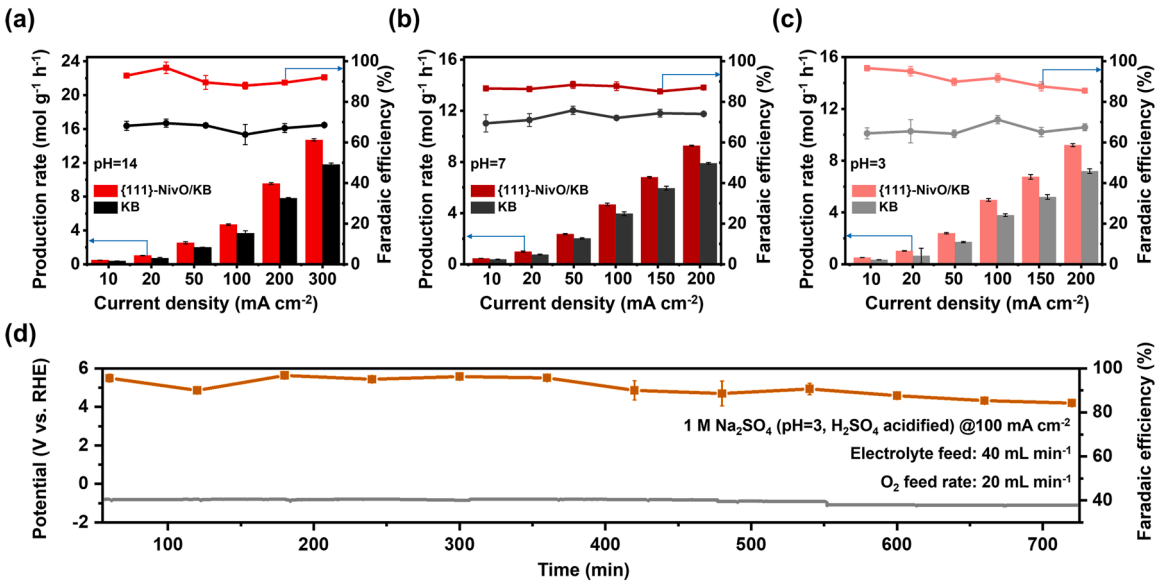

Fig. 5. H_2O_2 production performance measured by a flow cell. (a) Faradaic efficiency and H_2O_2 production under different current densities in 1 M KOH (pH=14). (b) Faradaic efficiency and H_2O_2 production rate of the catalyst measured under different current densities in 1 M Na_2SO_4 (pH=7). (c) Faradaic efficiency and H_2O_2 production rate of the catalyst measured under different current densities in 1 M H_2SO_4-regulated Na_2SO_4 (pH=3). (d) Stability test of the {111}-NivO/KB catalyst under 100 mA cm^{-2} in 1 M H_2SO_4-regulated Na_2SO_4 for 12 h (The electrolyte feeding rate was fixed at 40 mL h^{-1} and the O_2 feeding rate was fixed at 20 mL min^{-1} in the test).

3.5. *Highly concentrated wastewater treatment*

The in-situ H_2O_2 production through the electrochemical catalytic process finds a particularly valuable application in water treatment and environmental clean-up processes. To realize it, a flow cell-EF combined device that integrated the optimized {111}-NivO/KB cathode catalyst and EF process enables remarkable acceleration in decay time and speed for complete pollutant degradation Fig. 6a. Conventional EF devices, whether in a batch reaction or combined with a separated H-type cell, still face performance limitations in pollutant decomposition, largely due to the following reasons. First, H_2O_2 production is hindered by relying on the low concentration of dissolved O_2 within a finite current supply. Second, during prolonged operation in a non-circulating electrolyte environment, excessively trapped H_2O_2 faces the issue of self-decomposition or obstructs pollutant mineralization by converting ·OH into hydroperoxyl radicals (HO_2·) ($H_2O_2 + \cdot OH \rightarrow HO_2\cdot + H_2O$). Both scenarios detrimentally impact mineralization performance, leading to lower overall removal efficiency [10]. Consequently, the challenge of continuous H_2O_2 production in a static environment raises concerns about the suitability of the EF system for the efficient removal of phenolic pollutants. According to the performance summary of the recent state-of-the-art reported catalysts for the BPA removal by using an EF system (Table S11), it is found that fast removal is only achievable at low pollutant concentrations in limited wastewater volumes (less than 50 ppm in 100 mL). However, as pollutant concentration increases, processing time proportionally extends, hindering complete removal and falling short of industrialization expectations due to limited H_2O_2 production containment [17]. Thus, the development of a more advanced oxidation system is imperative to realize super-fast degradation and high TOC removal.

Impressively, as depicted in Fig. 6a, the integration of the flow cell system with the EF process, under optimal conditions, demonstrates remarkable performance (see more details about the optimization in Fig. S57 and **note S1**). As shown in Fig. 6b-d, the tests were conducted at room temperature in a 200 mL O_2-saturated acidified 1 M Na_2SO_4 solution with 50 mg L^{-1} bisphenol A (BPA), where the process is operated under a constant current of 400 mA with a 20 mL min^{-1} flowing rate of O_2. Here, {111}-NivO/KB was coated on the GDL with an optimal loading of 0.6 mg cm^{-2} as the $2e^-$ ORR electrocatalyst in the cathode part, facilitating efficient H_2O_2 production. Furthermore, 1.3 mM Fe^{2+} was added to the cathodic electrolyte as the EF catalyst. The results revealed a significant acceleration in both decay time and speed, achieving 100 % degradation of the high-concentration, large-volume BPA pollutant within 4 min by this advanced contaminant degradation device, which exhibits 102 times faster pseudo-first-order kinetics (k = 1.125 min^{-1}) compared to the traditional EF process (0.011 min^{-1}) under the same current during cell operation (400 mA) (Fig. 6b-d). Notably, under O_2-deficient conditions, where Ar was used as the inert gas in the cell, BPA degradation efficiency showed minimal variation (less than 15 %) under the applied current over 2 hours of operation. This indicates that the adsorption process on the electrode surfaces, induced by the applied current, had a negligible effect on pollutant removal (Fig. S58).

To assess the effect of added Fe^{2+} on H_2O_2 activation, we evaluated the performance of the {111}-NivO/KB catalyst for BPA decomposition under optimized Electro-Fenton conditions, both with and without Fe^{2+} (Fig. S59). Before applying a constant current of 400 mA, the catalyst alone achieved a BPA removal rate of approximately 10 % through adsorption. However, after applying the current for 2 hours, the in-situ production of H_2O_2 resulted in only negligible BPA degradation without any Fe^{2+} additive. Notably, when both H_2O_2 and Fe^{2+} species were present simultaneously, BPA decomposition was significantly accelerated, indicating the catalytic function of Fe^{2+} as an effective Electro-Fenton catalyst. To further investigate the oxidant produced by Fe^{2+}, radical quenching experiments using tert-butyl alcohol (TBA) were conducted to identify the reactive species, as TBA is known to have a high reaction rate with ·OH ($k = 3.8 \times 10^8$ M^{-1} s^{-1}).[63] As shown in Fig. S60, the degradation rate constant of BPA dropped significantly by over 60 % within 5 minutes in the presence of 0.005 mM TBA. The inhibitory effect on BPA decomposition became even more pronounced as the dose of TBA increased to 0.05 mM, resulting in only 23 % degradation. These findings strongly confirm that ·OH radicals play a key role in BPA decomposition via the Electro-Fenton reaction.

To elucidate the rapid pollutant removal in this advanced EF system, a careful examination of electrolyte flow, O_2 supply methods, and applied current density was conducted, around threefold higher kinetics

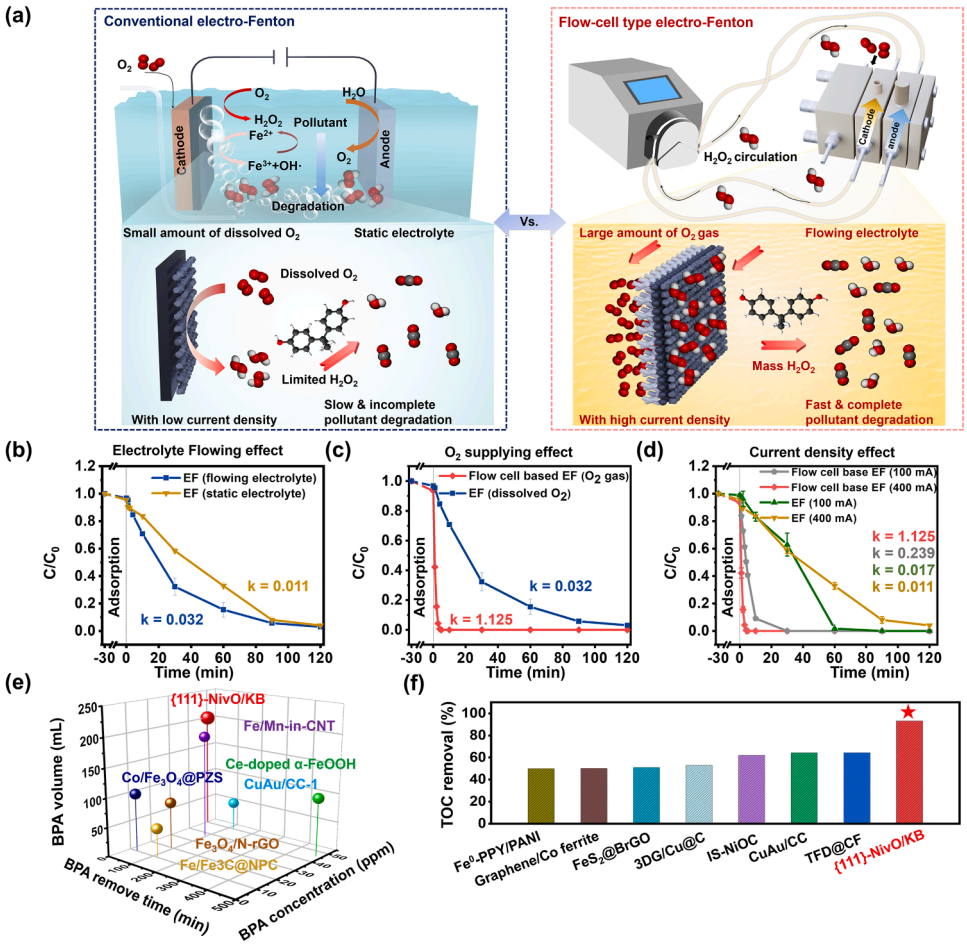

Fig. 6. Pollutant removal performance by a flow cell and electro-Fenton system combined advanced degradation system. (a) Schematic illustration of different BPA removal systems: conventional electro-Fenton (left), and flow cell type electro-Fenton (right). (b-d) BPA removal efficiency and pseudo-first-order reaction constant (k) by different effects on the above systems. (e) the comparison of the BPA removal performance (degradation times, BPA concentration, and volume) in flow cell type electro-Fenton system by using {111}-NivO/KB and other reported systems with various catalysts. (f) the TOC removal comparison of 50 ppm BPA with different reported catalysts (For all the experiments conducted here, the electrolyte flow rate was fixed at a constant 40 mL min^{-1}, and O_2 was supplied at 20 mL min^{-1}. The test involved treating a 200 mL solution containing 50 ppm BPA in 1 M Na_2SO_4, which was adjusted to pH 3 with H_2SO_4. Except for the experiment exploring the effect of current in section d, all other experiments were conducted under an applied current of 400 mA for comparison).

could be achieved due to not only the prevention of self-decomposed unstable H_2O_2 but also the avoidance of a side reaction between ·OH and H_2O_2 through the recycling of trapped H_2O_2 under electrolyte flow. It is noteworthy that H_2O_2 produced from dissolved O_2 in the electrolyte, via pre-purged O_2 gas in the EF system, is limited for effective pollutant degradation. For enhanced degradation speed, ensuring a sufficient concentration of O_2 is crucial. In the flow cell system, a continuous supply of highly concentrated O_2 occurs through fast O_2 gas penetration via the hydrophobic GDL into the catalyst surface. This results in 35 times faster kinetics compared to the electrolyte-flowing EF system, showing extensive H_2O_2 production enhancement. Moreover, applying higher currents accelerated the BPA pollutant removal in the flow cell-based EF. However, as mentioned earlier, the removal efficiency is reduced in conventional EF systems due to the instability and reactivity of excessively captured H_2O_2 at high current density (Fig. 6d). For further comparison, a conventional EF with the generally applied current of 15 mA was also used for further confirmation of the effect of applied current. As the results in Fig. S61a-b reveal, the conventional EF with 15 mA applied current showed higher kinetics (k=0.231 min^{-1}) compared to 100 mA (0.017 min^{-1}) and 400 mA (0.011 min^{-1}). Nevertheless, limited H_2O_2 production under low current density hinders the complete removal of highly concentrated BPA within a short period. As expected, the TOC in the EF system is only approximately 40 % during the 2 -hour operation. In contrast, 93 % TOC removal can be accomplished by the flow cell EF due to a combination of continuously producing large amounts of H_2O_2 under applied high current by supplying abundant O_2 gas and simultaneous expulsion of excessive H_2O_2 (Fig. S61c). This highly effective assembly process in both removal speed and mineralization level of the numerous pollutants with high concentration surpasses all the other well-designed systems and catalysts in the literature to date (Fig. 6e and Table S11).

To compare the effectiveness of the {111}-NivO/KB catalyst in the advanced flow cell EF, the same BPA degradation test was evaluated utilizing pure KB for 2 hours under optimal conditions. It is found that even though fast removal speed of within 4 minutes was still achieved for both KB and for{100}-NiO/KB, the TOC removal reached only 45 % and 65.1 % after 2 hours of cell operation, due to the lower H_2O_2 production efficiency (averaging 60 % for KB, 80 % for {100}-NivO/KB, and 90 % for {111}-NivO/KB) in acidic conditions (Fig. S62). Also, to explore the effect of the electrocatalytic materials on the system, the EF recycling test was also run without adding any BPA pollutant inside of the cathodic electrolyte (a pH=3 of 200 mL of 1 M H_2SO_4-regulated Na_2SO_4 electrolytes with the addition of 1.3 mM Fe^{2+}) to directly check the stability of H_2O_2 production performance under every 2-hour operation. The catalytic surface underwent continuous degradation due to the long-term chemisorption and aging of the produced •OH on

the KB catalyst. Additionally, when carbon materials are employed as cathodes, the oxygen atoms present on the carbon surface can be removed by electrons under reducing potentials, leading to the loss of some active oxygen-containing functional groups, such as carboxyl species, which are crucial for catalytic activity [64–66]. For this reason, the FE of KB falls faster than {111}-NivO/KB during the cycling measurement. These results thus demonstrate the better performance and stability of {111}-NivO/KB as the electrocatalyst in the advanced oxidation system than KB (Fig. S63).

To evaluate the reusability and stability of the {111}-NivO/KB catalyst for potential applications in the flow cell electro-Fenton system, we conducted cycling tests for 5 cycles using the same electrode. After each cycle, the electrode was collected, rinsed with DI water, and dried in an oven at 60 ºC overnight for reuse in subsequent cycles. As shown in Fig. S64, there was a negligible reduction in BPA decomposition efficiency, with only a minor decrease in H_2O_2 yield and Faradic efficiency after 5 cycles. Additionally, the Ni leaching concentration was below the problematic level (< 0.2 mg kg^{-1}), which is well within the standard for industrial wastewater discharged into inland waters (< 3 ppm) [67]. This was determined by analyzing the post-reaction solution using inductively coupled plasma mass spectrometry (ICP-MS). SEM images of the used catalyst, displayed in Fig. S65, show no significant changes in morphology, indicating that the catalyst was well-preserved. These results demonstrate that the {111}-NivO/KB catalyst is stable and effective for continuous H_2O_2 supply in the electro-Fenton reaction.

Additionally, this optimal design also demonstrates distinct advantages in pollutant removal compared to well-designed catalyst and purification processes (Fig. 6f and Table S12). Under this recycling system, persistent pollutant elimination was implemented, which could be further expanded into other heavy pollutants, such as phenol. As confirmed, the system attains 84.9 % TOC removal with 10–30 times faster kinetics for 200 mL of 50 ppm phenol degradation, owing to the remarkable performance among the well-reported cases (Fig. S66 and Table S13). This high-performance material and system technology opens up new possibilities for wastewater treatment.

4. Conclusions

The exposed crystal facet and high-valent cation vacancies on the NiO surface can be systematically manipulated by tuning the condition of a used precipitant agent, heat treatment temperature, and heating rate. As a result, we successfully synthesized NiO catalysts with exposed (111) domain crystal facets and Niv with excellent $2e^-$ ORR performance. Combined with the DFT simulations, the NiO with a (111) crystal plane exposed surface and abundant high valence state defects (Ni^{3+}), {111}-NivO, was shown to possess highly optimal binding energy for the $2e^-$ ORR process. At 0.65 V vs. RHE in an alkaline solution, this top-performing catalyst could achieve excellent balanced catalytic performance with up to 96 % ultrahigh selectivity with high mass activity of 59 A g^{-1} due to the existence of highly exposed active sites Ni^{3+} on the (111) plane with high concentration, which was 23 % greater than the (100) facet domain stoichiometric NiO reference. The observed enhancement in catalytic activity for the {111}-NivO case is substantiated by DFT results, which indicate that an increased number of Niv on the Ni-terminated NiO (111) surface leads to a weaker binding affinity of the *OOH intermediate, thereby confirming improved performance. In a flow cell device for the H_2O_2 mass production with this catalyst, over 85 % faradaic efficiencies were achieved at all pH conditions and the catalyst maintained this high level of efficiency over an extended period of operation, demonstrating excellent stability. Additionally, in only 4 min, by combining flow cell technology with the EF technique, 100 % removal of a 200 mL solution of 50 ppm BPA was accomplished at a more than a hundred times faster rate ($k = 1.125$ min^{-1}) than with the conventionally used EF system. Mineralization was also very high with a 93 % TOC reduction in two hours. The rapid removal of BPA is achieved not only by the continuous and adequate supply of large amounts of H_2O_2 along with the flow of O_2 gas under high current density conditions but also by the contributions from the timely recycling of excessive trapped H_2O_2 through electrolyte cycling. Furthermore, the robust and active inorganic-based {111}-NivO catalyst exhibited better durability and performance in the advanced Fenton system than pure carbon black catalyst. Our findings open up new possibilities for high-efficiency wastewater treatment in decentralized or remote areas.

CRediT authorship contribution statement

Wenjun Zhang: Conceptualization, Investigation, Formal Analysis, Writing - original draft. **Thao Thi Le:** Investigation, Formal Analysis, Resources. **Dongyup Shin:** Conceptualization, Investigation, Software, Writing - original draft. **Subhajit Nandy:** Resources, Methodology. **Jae Won Choi:** Resources, Methodology. **Sae Yane Paek:** Resources, Methodology. **Chang-Kyu Hwang:** Resources, Methodology. **Jin Hyueng Kim:** Resources, Methodology. **Hoyoung Suh:** Resources, Methodology. **Keun Hwa Chae:** Resources, Methodology. **Seung Yong Lee:** Resources, Methodology. **Sang Soo Han:** Writing - review & editing, Funding acquisition. **Sang Hoon Kim:** Writing - review & editing, Funding acquisition. **Jong Min Kim:** Conceptualization, Writing - review & editing, Supervision, Funding acquisition, Project administration.

Declaration of Competing Interest

The authors declare the following financial interests/personal relationships which may be considered as potential competing interests: Jong Min Kim & Sang Soo Han reports financial support was provided by National Research Foundation of Korea. Sang Hoon Kim reports financial support was provided by Korea Ministry of Environment. Wenjun Zhang reports financial support was provided by University of Science and Technology. If there are other authors, they declare that they have no known competing financial interests or personal relationships that could have appeared to influence the work reported in this paper.

Data availability

Data will be made available on request.

Acknowledgements

The research work was supported by the KIST Institutional Programs [2E33241, 2E33171]; the National Research Foundation of Korea (NRF) grant funded by the Korea government (MSIT) [No. RS-2023-00209940 and NRF-2022M3H4A7046278]; Korea Environment Industry & Technology Institute (KEITI) funded by Korea Ministry of Environment (MOE) [2021002800005]. This work was also supported by the project fund of the 2022 UST Young Scientist + Research Program of the University of Science and Technology (UST) [No. 2022YS24].

Appendix A. Supporting information

Supplementary data associated with this article can be found in the online version at doi:10.1016/j.apcatb.2024.124666.

References

[1] T. Deblonde, C. Cossu-Leguille, P. Hartemann, Emerging pollutants in wastewater: a review of the literature, Int. J. Hyg. Environ. Health 214 (2011) 442–448, https://doi.org/10.1016/j.ijheh.2011.08.002.

[2] M.A. La Merrill, L.N. Vandenberg, M.T. Smith, W. Goodson, P. Browne, H. B. Patisaul, K.Z. Guyton, A. Kortenkamp, V.J. Cogliano, T.J. Woodruff, L. Rieswijk, H. Sone, K.S. Korach, A.C. Gore, L. Zeise, R.T. Zoeller, Consensus on the key characteristics of endocrine-disrupting chemicals as a basis for hazard identification, Nat. Rev. Endocrinol. 16 (2020) 45–57, https://doi.org/10.1038/s41574-019-0273-8.

[3] A.C. Gore, V.A. Chappell, S.E. Fenton, J.A. Flaws, A. Nadal, G.S. Prins, J. Toppari, R.T. Zoeller, EDC-2: the endocrine society's second scientific statement on endocrine-disrupting chemicals, Endocr. Rev. 36 (2015) E1–E150, https://doi.org/10.1210/er.2015-1010.

[4] E.J. Inam, I.B. Nwoke, E.D. Udosen, N.-A.O. Offiong, Ecological risks of phenolic endocrine disrupting compounds in an urban tropical river, Environ. Sci. Pollut. Res. 26 (2019) 21589–21597, https://doi.org/10.1007/s11356-019-05458-7.

[5] A. Tarafdar, R. Sirohi, P.A. Balakumaran, R. Reshmy, A. Madhavan, R. Sindhu, P. Binod, Y. Kumar, D. Kumar, S.J. Sim, The hazardous threat of Bisphenol A: toxicity, detection and remediation, J. Hazard. Mater. 423 (2022) 127097, https://doi.org/10.1016/j.jhazmat.2021.127097.

[6] J. Du, J. Bao, X. Fu, C. Lu, S.H. Kim, Mesoporous sulfur-modified iron oxide as an effective Fenton-like catalyst for degradation of bisphenol A, Appl. Catal. B Environ. 184 (2016) 132–141, https://doi.org/10.1016/j.apcatb.2015.11.015.

[7] Y. Zhang, Z. Chen, P. Wu, Y. Duan, L. Zhou, Y. Lai, F. Wang, S. Li, Three-dimensional heterogeneous Electro-Fenton system with a novel catalytic particle electrode for Bisphenol A removal, J. Hazard. Mater. 393 (2020) 120448, https://doi.org/10.1016/j.jhazmat.2019.03.067.

[8] F.-X. Wang, C.-C. Wang, X. Du, Y. Li, F. Wang, P. Wang, Efficient removal of emerging organic contaminants via photo-Fenton process over micron-sized Fe-MOF sheet, Chem. Eng. J. 429 (2022) 132495, https://doi.org/10.1016/j.cej.2021.132495.

[9] T.T. Le, V.C. Hoang, W. Zhang, J.M. Kim, J. Kim, G. Moon, S.H. Kim, Mesoporous sulfur-modified metal oxide cathodes for efficient electro-Fenton systems, Chem. Eng. J. Adv. 12 (2022) 100371, https://doi.org/10.1016/j.ceja.2022.100371.

[10] E. Brillas, I. Sirés, M.A. Oturan, Electro-Fenton process and related electrochemical technologies based on Fenton's reaction chemistry, Chem. Rev. 109 (2009) 6570–6631, https://doi.org/10.1021/cr900136g.

[11] Z. Luo, M. Liu, D. Tang, Y. Xu, H. Ran, J. He, K. Chen, J. Sun, High H_2O_2 selectivity and enhanced Fe2+ regeneration toward an effective electro-Fenton process based on a self-doped porous biochar cathode, Appl. Catal. B Environ. 315 (2022) 121523, https://doi.org/10.1016/j.apcatb.2022.121523.

[12] S.O. Ganiyu, M. Zhou, C.A. Martínez-Huitle, Heterogeneous electro-Fenton and photoelectro-Fenton processes: a critical review of fundamental principles and application for water/wastewater treatment, Appl. Catal. B Environ. 235 (2018) 103–129, https://doi.org/10.1016/j.apcatb.2018.04.044.

[13] F. Deng, H. Olvera-Vargas, M. Zhou, S. Qiu, I. Sirés, E. Brillas, Critical review on the mechanisms of Fe2+ regeneration in the electro-fenton process: fundamentals and boosting strategies, Chem. Rev. 123 (2023) 4635–4662, https://doi.org/10.1021/acs.chemrev.2c00684.

[14] M. Melchionna, P. Fornasiero, M. Prato, The rise of hydrogen peroxide as the main product by metal-free catalysis in oxygen reductions, Adv. Mater. 31 (2019) 1802920, https://doi.org/10.1002/adma.201802920.

[15] H. Sheng, A.N. Janes, R.D. Ross, D. Kaiman, J. Huang, B. Song, J.R. Schmidt, S. Jin, Stable and selective electrosynthesis of hydrogen peroxide and the electro-Fenton process on $CoSe_2$ polymorph catalysts, Energy Environ. Sci. 13 (2020) 4189–4203, https://doi.org/10.1039/D0EE01925A.

[16] M. Sun, X.-R. Ru, L.-F. Zhai, In-situ fabrication of supported iron oxides from synthetic acid mine drainage: high catalytic activities and good stabilities towards electro-Fenton reaction, Appl. Catal. B Environ. 165 (2015) 103–110, https://doi.org/10.1016/j.apcatb.2014.09.077.

[17] P.V. Nidheesh, C. Trellu, H.O. Vargas, E. Mousset, S.O. Ganiyu, M.A. Oturan, Electro-Fenton process in combination with other advanced oxidation processes: challenges and opportunities, Curr. Opin. Electrochem. 37 (2023) 101171, https://doi.org/10.1016/j.coelec.2022.101171.

[18] Y. Bu, Y. Wang, G.-F. Han, Y. Zhao, X. Ge, F. Li, Z. Zhang, Q. Zhong, J.-B. Baek, Carbon-based electrocatalysts for efficient hydrogen peroxide production, Adv. Mater. 33 (2021) 2103266, https://doi.org/10.1002/adma.202103266.

[19] F. Xiang, X. Zhao, J. Yang, N. Li, W. Gong, Y. Liu, A. Burguete-Lopez, Y. Li, X. Niu, A. Fratalocchi, Enhanced selectivity in the electroproduction of H_2O_2 via F/S dual-doping in metal-free nanofibers, Adv. Mater. 35 (2023) 2208533, https://doi.org/10.1002/adma.202208533.

[20] A. Byeon, W.C. Yun, J.M. Kim, J.W. Lee, Recent progress in heteroatom-doped carbon electrocatalysts for the two-electron oxygen reduction reaction, Chem. Eng. J. 456 (2023) 141042, https://doi.org/10.1016/j.cej.2022.141042.

[21] A. Byeon, W.C. Yun, J.M. Kim, J.W. Lee, Non-precious metal catalysts for two-electron oxygen reduction reaction, ChemElectroChem 10 (2023) e202300234, https://doi.org/10.1002/celc.202300234.

[22] H. He, S. Liu, Y. Liu, L. Zhou, H. Wen, R. Shen, H. Zhang, X. Guo, J. Jiang, B. Li, Review and perspectives on carbon-based electrocatalysts for the production of H 2 O 2 via two-electron oxygen reduction, Green. Chem. 25 (2023) 9501–9542, https://doi.org/10.1039/D3GC02856A.

[23] L. Xin, J. Hu, Y. Xiang, C. Li, L. Fu, Q. Li, X. Wei, Carbon-based nanocomposites as fenton-like catalysts in wastewater treatment applications: a review, Materials 14 (2021) 2643, https://doi.org/10.3390/ma14102643.

[24] S. Wang, Y. Chu, C. Lan, C. Liu, J. Ge, W. Xing, Metal–nitrogen–carbon catalysts towards acidic ORR in PEMFC: fundamentals, durability challenges, and improvement strategies, Chem. Synth. 3 (2023) 15, https://doi.org/10.20517/cs.2022.36.

[25] Y. Zhang, H. Jiang, C. Zhang, Y. Feng, H. Feng, S. Zhu, J. Hu, High-efficiency oxygen reduction by late transition metal oxides to produce H_2O_2, J. Mater. Chem. A 12 (2024) 6123–6133, https://doi.org/10.1039/D3TA06995H.

[26] N. Wang, S. Ma, P. Zuo, J. Duan, B. Hou, Recent progress of electrochemical production of hydrogen peroxide by two-electron oxygen reduction reaction, Adv. Sci. 8 (2021) 2100076, https://doi.org/10.1002/advs.202100076.

[27] H. Li, S. Kelly, D. Guevarra, Z. Wang, Y. Wang, J.A. Haber, M. Anand, G.T.K. K. Gunasooriya, C.S. Abraham, S. Vijay, J.M. Gregoire, J.K. Nørskov, Analysis of the limitations in the oxygen reduction activity of transition metal oxide surfaces, Nat. Catal. 4 (2021) 463–468, https://doi.org/10.1038/s41929-021-00618-w.

[28] D. Banham, T. Kishimoto, Y. Zhou, T. Sato, K. Bai, J. Ozaki, Y. Imashiro, S. Ye, Critical advancements in achieving high power and stable nonprecious metal catalyst–based MEAs for real-world proton exchange membrane fuel cell applications, Sci. Adv. 4 (2018) eaar7180, https://doi.org/10.1126/sciadv.aar7180.

[29] G. Wu, W. Chen, X. Zheng, D. He, Y. Luo, X. Wang, J. Yang, Y. Wu, W. Yan, Z. Zhuang, X. Hong, Y. Li, Hierarchical Fe-doped NiO_x nanotubes assembled from ultrathin nanosheets containing trivalent nickel for oxygen evolution reaction, Nano Energy 38 (2017) 167–174, https://doi.org/10.1016/j.nanoen.2017.05.044.

[30] Y. Wang, R. Shi, L. Shang, G.I.N. Waterhouse, J. Zhao, Q. Zhang, L. Gu, T. Zhang, High-efficiency oxygen reduction to hydrogen peroxide catalyzed by nickel single-atom catalysts with tetradentate N_2O_2 coordination in a three-phase flow cell, Angew. Chem. Int. Ed. 59 (2020) 13057–13062, https://doi.org/10.1002/anie.202004841.

[31] Y. Yan, J. Lin, T. Xu, B. Liu, K. Huang, L. Qiao, S. Liu, J. Cao, S.C. Jun, Y. Yamauchi, J. Qi, Atomic-level platinum filling into Ni-vacancies of dual-deficient NiO for boosting electrocatalytic hydrogen evolution, Adv. Energy Mater. 12 (2022) 2200434, https://doi.org/10.1002/aenm.202200434.

[32] S. Geng, J. Yujin, S.-Z. Yang, J. Su, Z. Hu, T. Chan, H. Yu, Y. Li, Y. Chin, X. Huang, Q. Shao, Phosphorus optimized metastable hexagonal-close-packed phase nickel for efficient hydrogen peroxide production in neutral media, Adv. Funct. Mater. 33 (2023) 2300636, https://doi.org/10.1002/adfm.202300636.

[33] R. Li, S. Yang, Y. Zhang, G. Yu, C. Wang, C. Chen, G. Wu, R. Sun, G. Wang, X. Zheng, W. Yan, G. Wang, D. Rao, X. Hong, Short-range order in amorphous nickel oxide nanosheets enables selective and efficient electrochemical hydrogen peroxide production, Cell Rep. Phys. Sci. 3 (2022) 100788, https://doi.org/10.1016/j.xcrp.2022.100788.

[34] Z. Wu, T. Wang, J.-J. Zou, Y. Li, C. Zhang, Amorphous nickel oxides supported on carbon nanosheets as high-performance catalysts for electrochemical synthesis of hydrogen peroxide, ACS Catal. (2022) 5911–5920, https://doi.org/10.1021/acscatal.2c01829.

[35] N. Kitakatsu, V. Maurice, P. Marcus, Local decomposition of NiO ultra-thin films formed on Ni(111), Surf. Sci. 411 (1998) 215–230, https://doi.org/10.1016/S0039-6028(98)00372-0.

[36] C.A. Cadigan, A.R. Corpuz, F. Lin, C.M. Caskey, K.B.H. Finch, X. Wang, R. M. Richards, Nanoscale (111) faceted rock-salt metal oxides in catalysis, Catal. Sci. Technol. 3 (2013) 900–911, https://doi.org/10.1039/C2CY20373A.

[37] Y. Yan, J. Zhong, R. Wang, S. Yan, Z. Zou, Trivalent nickel-catalyzing electroconversion of alcohols to carboxylic acids, J. Am. Chem. Soc. 146 (2024) 4814–4821, https://doi.org/10.1021/jacs.3c13155.

[38] X. Xu, H. Zhang, Y. Tong, Y. Sun, X. Fang, J. Xu, X. Wang, Tuning Ni^{3+} quantity of NiO via doping of cations with varied valence states: the key role of Ni^{3+} on the reactivity, Appl. Surf. Sci. 550 (2021) 149316, https://doi.org/10.1016/j.apsusc.2021.149316.

[39] M. Steimecke, G. Seiffarth, C. Schneemann, F. Oehler, S. Förster, M. Bron, Higher-valent nickel oxides with improved oxygen evolution activity and stability in alkaline media prepared by high-temperature treatment of $Ni(OH)_2$, ACS Catal. 10 (2020) 3595–3603, https://doi.org/10.1021/acscatal.9b04788.

[40] M.S.N. K, C. Alex, R. Jana, A. Datta, N.S. John, Remarkable CO_x tolerance of Ni^{3+} active species in a Ni_2O_3 catalyst for sustained electrochemical urea oxidation, J. Mater. Chem. A 10 (2022) 4209–4221, https://doi.org/10.1039/D1TA05753G.

[41] Z. Zhou, Y. Kong, H. Tan, Q. Huang, C. Wang, Z. Pei, H. Wang, Y. Liu, Y. Wang, S. Li, X. Liao, W. Yan, S. Zhao, Cation-vacancy-enriched nickel phosphide for efficient electrosynthesis of hydrogen peroxides, Adv. Mater. 34 (2022) 2106541, https://doi.org/10.1002/adma.202106541.

[42] K. Nair, V. Kumaravel, S. Pillai, Carbonaceous cathode materials for electro-Fenton technology: mechanism, kinetics, recent advances, opportunities and challenges, Chemosphere 269 (2020) 129325, https://doi.org/10.1016/j.chemosphere.2020.129325.

[43] W. Zhang, J.W. Choi, S. Kim, T.T. Le, S. Nandy, C.-K. Hwang, S.Y. Paek, A. Byeon, K.H. Chae, S.Y. Lee, S.H. Kim, H. Song, J. Kim, J. Oh, J.W. Lee, S.S. Han, J.M. Kim, Penta nitrogen coordinated cobalt single atom catalysts with oxygenated carbon black for electrochemical H_2O_2 production, Appl. Catal. B Environ. 331 (2023) 122712, https://doi.org/10.1016/j.apcatb.2023.122712.

[44] A. Byeon, J.W. Choi, H.W. Lee, W.C. Yun, W. Zhang, C.-K. Hwang, S.Y. Lee, S. S. Han, J.M. Kim, J.W. Lee, CO_2-derived edge-boron-doped hierarchical porous carbon catalysts for highly effective electrochemical H_2O_2 production, Appl. Catal. B Environ. 329 (2023) 122557, https://doi.org/10.1016/j.apcatb.2023.122557.

[45] H. Sheng, E.D. Hermes, X. Yang, D. Ying, A.N. Janes, W. Li, J.R. Schmidt, S. Jin, Electrocatalytic production of H_2O_2 by selective oxygen reduction using earth-abundant cobalt pyrite (CoS_2), ACS Catal. 9 (2019) 8433–8442, https://doi.org/10.1021/acscatal.9b02546.

[46] B. Zhao, X.-K. Ke, J.-H. Bao, C.-L. Wang, L. Dong, Y.-W. Chen, H.-L. Chen, Synthesis of flower-like NiO and effects of morphology on its catalytic properties, J. Phys. Chem. C. 113 (2009) 14440–14447, https://doi.org/10.1021/jp904186k.

[47] W.-B. Zhang, N. Yu, W.-Y. Yu, B.-Y. Tang, Stability and magnetism of vacancy in NiO: a GGA+*U* study, Eur. Phys. J. B 64 (2008) 153–158, https://doi.org/10.1140/epjb/e2008-00303-x.

[48] G. Tyuliev, M. Sokolova, Temperature dependence of Ni^{3+} quantity in the surface layer of NiO, Appl. Surf. Sci. 52 (1991) 343–349, https://doi.org/10.1016/0169-4332(91)90078-X.

[49] J. Zhang, D. Zeng, Q. Zhu, J. Wu, Q. Huang, C. Xie, Effect of nickel vacancies on the room-temperature NO2 sensing properties of mesoporous NiO nanosheets, J. Phys. Chem. C. 120 (2016) 3936–3945, https://doi.org/10.1021/acs.jpcc.5b12162.
[50] Y.-H. Lee, J.W. Corbett, EPR studies of defects in electron-irradiated silicon: a triplet state of vacancy-oxygen complexes, Phys. Rev. B 13 (1976) 2653–2666, https://doi.org/10.1103/PhysRevB.13.2653.
[51] T. Xu, D. Jiao, M. Liu, L. Zhang, X. Fan, L. Zheng, W. Zheng, X. Cui, Ni center coordination reconstructed nanocorals for efficient water splitting, Adv. Sci. 10 (2023) 2205605, https://doi.org/10.1002/advs.202205605.
[52] S. Park, H.-S. Ahn, C.-K. Lee, H. Kim, H. Jin, H.-S. Lee, S. Seo, J. Yu, S. Han, Interaction and ordering of vacancy defects in NiO, Phys. Rev. B 77 (2008) 134103, https://doi.org/10.1103/PhysRevB.77.134103.
[53] D.-Y. Cho, S.Ji Song, U.Ki Kim, K.Min Kim, H.-K. Lee, C.Seong Hwang, Spectroscopic investigation of the hole states in Ni-deficient NiO films, J. Mater. Chem. C. 1 (2013) 4334–4338, https://doi.org/10.1039/C3TC30687A.
[54] A. Anspoks, A. Kalinko, R. Kalendarev, A. Kuzmin, Atomic structure relaxation in nanocrystalline NiO studied by EXAFS spectroscopy: role of nickel vacancies, Phys. Rev. B 86 (2012) 174114, https://doi.org/10.1103/PhysRevB.86.174114.
[55] T.R. Silva, V.D. Silva, L.S. Ferreira, A.J.M. Araújo, M.A. Morales, T.A. Simões, C. A. Paskocimas, D.A. Macedo, Role of oxygen vacancies on the energy storage performance of battery-type NiO electrodes, Ceram. Int. 46 (2020) 9233–9239, https://doi.org/10.1016/j.ceramint.2019.12.176.
[56] Y. Qi, H. Qi, C. Lu, Y. Yang, Y. Zhao, Photoluminescence and magnetic properties of β-Ni(OH)2 nanoplates and NiO nanostructures, J. Mater. Sci. Mater. Electron. 20 (2009) 479–483, https://doi.org/10.1007/s10854-008-9755-5.
[57] N. Lahiri, D. Song, X. Zhang, X. Huang, K.A. Stoerzinger, O.Q. Carvalho, P.P. Adiga, M. Blum, K.M. Rosso, Interplay between facets and defects during the dissociative and molecular adsorption of water on metal oxide surfaces, J. Am. Chem. Soc. 145 (2023) 2930–2940, https://doi.org/10.1021/jacs.2c11291.
[58] J. Filippi, H.A. Miller, L. Nasi, M.V. Pagliaro, A. Marchionni, M. Melchionna, P. Fornasiero, F. Vizza, Optimization of H_2O_2 production in a small-scale off-grid buffer layer flow cell equipped with Cobalt@N-doped graphitic carbon core–shell nanohybrid electrocatalyst, Mater. Today Energy 29 (2022) 101092, https://doi.org/10.1016/j.mtener.2022.101092.
[59] C. Xiao, L. Cheng, Y. Zhu, G. Wang, L. Chen, Y. Wang, R. Chen, Y. Li, C. Li, Super-coordinated nickel $N_4Ni_1O_2$ site single-atom catalyst for selective h2o2 electrosynthesis at high current densities, Angew. Chem. Int. Ed. 61 (2022) e202206544, https://doi.org/10.1002/anie.202206544.
[60] Y. Wu, H. Ma, Y. Feng, Z. Shi, Y. Yi, Y. Ding, J. Feng, W. Zhao, J. Sun, S. Dong, J. Sun, Harnessing optimized surface reconstruction of single-atom Ni-doped Ni-NiO/NC precatalysts toward robust H_2O_2 production, ACS Appl. Mater. Interfaces 14 (2022) 26803–26813, https://doi.org/10.1021/acsami.2c05622.
[61] Y. Tong, J. Liu, B.-J. Su, J.-Y. Juang, F. Hou, L. Yin, S.X. Dou, J. Liang, High-rate electrochemical H_2O_2 production over multimetallic atom catalysts under acidic–neutral conditions, Carbon Energy 6 (2024) e378, https://doi.org/10.1002/cey2.378.
[62] J. Liang, Y. Wang, Q. Liu, Y. Luo, T. Li, H. Zhao, S. Lu, F. Zhang, A.M. Asiri, F. Liu, D. Ma, X. Sun, Electrocatalytic hydrogen peroxide production in acidic media enabled by NiS2 nanosheets, J. Mater. Chem. A 9 (2021) 6117–6122, https://doi.org/10.1039/D0TA12008A.
[63] X. Chen, W.-D. Oh, T.-T. Lim, Graphene- and CNTs-based carbocatalysts in persulfates activation: material design and catalytic mechanisms, Chem. Eng. J. 354 (2018) 941–976, https://doi.org/10.1016/j.cej.2018.08.049.
[64] L. Rojas, A. Peraza, F. Ruette, Aging oxidation reactions on atmospheric black carbon by OH radicals. A theoretical modeling study, J. Phys. Chem. A 119 (2015) 13038–13047, https://doi.org/10.1021/acs.jpca.5b07073.
[65] Y. Wang, W. Zhou, J. Gao, Y. Ding, K. Kou, Oxidative modification of graphite felts for efficient H_2O_2 electrogeneration: enhancement mechanism and long-term stability, J. Electroanal. Chem. 833 (2019) 258–268, https://doi.org/10.1016/j.jelechem.2018.11.051.
[66] N. Li, C. Huang, X. Wang, Y. Feng, J. An, Electrosynthesis of hydrogen peroxide via two-electron oxygen reduction reaction: a critical review focus on hydrophilicity/hydrophobicity of carbonaceous electrode, Chem. Eng. J. 450 (2022) 138246, https://doi.org/10.1016/j.cej.2022.138246.
[67] S. Song, M. Wu, Y. Liu, Q. Zhu, P. Tsiakaras, Y. Wang, Efficient and stable carbon-coated nickel foam cathodes for the electro-fenton process, Electrochim. Acta 176 (2015) 811–818, https://doi.org/10.1016/j.electacta.2015.07.029.